AGU ADVANCING EARTH AND SPACE SCIENCES

Geochemistry, Geophysics, Geosystems®

RESEARCH ARTICLE
10.1029/2025GC012446

Key Points:

- Seismic and geodetic data reveal deformation in the Peloritani Mts and Aeolian Archipelago, driven by tectonic forces and fluid circulation
- The Peloritani Mts area is affected by fluid–induced fault reactivations within a regional crustal scale strike–slip fault regime
- Fluids at near lithostatic pressures infiltrated fault zones, weakening the faults and triggering low–magnitude seismicity for 9 months

Supporting Information:

Supporting Information may be found in the online version of this article.

Correspondence to:

D. Messina,
danilo.messina@ingv.it

Citation:

Messina, D., Corradino, M., Barberi, G., Bruno, V., Mattia, M., Patanè, D., et al. (2026). Fluid-induced fault reactivations in strike-slip regimes: Temporal constraints from GNSS and seismological analysis in the Peloritani Mts and Aeolian Archipelago (Central Mediterranean). *Geochemistry, Geophysics, Geosystems*, *27*, e2025GC012446. https://doi.org/10.1029/2025GC012446

Received 27 MAY 2025
Accepted 22 NOV 2025

Author Contributions:

Conceptualization: Danilo Messina, Marta Corradino, Valentina Bruno, Mario Mattia, Fabrizio Pepe
Data curation: Danilo Messina, Graziella Barberi, Valentina Bruno, Mario Mattia, Domenico Patanè, Massimo Rossi, Luciano Scarfì
Formal analysis: Danilo Messina
Writing – original draft: Danilo Messina, Marta Corradino, Graziella Barberi, Luciano Scarfì

Fluid-Induced Fault Reactivations in Strike-Slip Regimes: Temporal Constraints From GNSS and Seismological Analysis in the Peloritani Mts and Aeolian Archipelago (Central Mediterranean)

Danilo Messina[1,2], Marta Corradino[2], Graziella Barberi[1], Valentina Bruno[1], Mario Mattia[1], Domenico Patanè[1], Massimo Rossi[1], Luciano Scarfì[1], and Fabrizio Pepe[2]

[1]Istituto Nazionale di Geofisica e Vulcanologia, Sezione di Catania—OE, Catania, Italy, [2]Dipartimento di Scienze della Terra e del Mare, Università di Palermo, Palermo, Italy

Abstract Fluids can modify the mechanical properties of rocks, including shear strength and strain behavior. We investigate the timing and magnitude of seismic events during fault motion in strike–slip systems across the Peloritani Mountains (northeastern Sicily) and Aeolian Archipelago using GNSS and seismological data analysis. Results reveal a strain partitioning along the already known crustal–scale NNW–SSE trending right–lateral transtensional deformation zone across the Peloritani Mts and its offshore extension up to Vulcano Island (defined as the Aeolian–Tindari–Letojanni Fault System, ATLFS), and WNW–ESE to NW–SE right–lateral transfer zones located in the western and central sectors of the Aeolian Archipelago. During 2021, the eastern block of the ATLFS underwent a significant velocity increase relative to the fixed western block, varying from 1.6 ± 0.28 mm/y (pre–2021 baseline) to 3.3 ± 0.99 mm/y. The acceleration of the eastern block of the ATLFS was accompanied by increased seismic strain release. It temporally correlated with the fastest ground inflation on Vulcano Island (central Aeolian Archipelago), which in turn coincided with the highest CO_2 flux emission on the island. This correlation, along with evidence of gas emissions in the Peloritani Mts, suggests that enhanced fluid pressure lubricated fault surfaces, thereby facilitating slip along the ATLFS. The fluid–induced slip acceleration was sustained for 9 months and was marked by frequent low–magnitude earthquakes.

Plain Language Summary Underground fluids can lubricate faults in the Earth's crust, reducing friction and enabling rock blocks to slide more easily. To investigate this process, we combined GNSS measurements with relocated earthquake hypocenters in the Peloritani Mountains of northeastern Sicily and the adjacent Aeolian archipelago. Our analysis has identified crustal deformation zones along the Peloritani Mts and its offshore extension up to the Volcano Island (defined as the Aeolian–Tindari–Letojanni Fault System, ATLFS), as well as in the western and central sectors of the Aeolian archipelago. In 2021, the eastern block of the ATLFS accelerated relative to its western counterpart, coinciding with an increase in seismic strain release in the Peloritani Mts area. At the same time, Vulcano's volcanic edifice underwent rapid ground inflation accompanied by a significant and unusual increase in CO_2 emission. The close temporal alignment of these four phenomena accelerated fault slip, increased seismic strain release, volcanic ground inflation, and elevated CO_2 emissions combined with evidence of gas discharge in the Peloritani area, indicates that enhanced fluid circulation lubricated the fault surface and facilitated sustained strain release along the ATLFS.

1. Introduction

Ground deformations exhibit distinct spatial and temporal changes as tectonic systems transition through stress accumulation to strain release. Seismic strain release involves redistributing accumulated tectonic stress by displacing crustal blocks along fault planes. This process occurs during both co–seismic and post–seismic phases. Typically, co-seismic events refer to rapid strain release along a fault plane, lasting seconds to minutes, which can lead to measurable deformation on the surface. Post-seismic deformation can persist for days to years, releasing residual strain due to the ongoing adjustment of the crust in response to the stress drop. Fault geometry, stress field orientations, and material properties collectively govern the initiation, propagation, and termination of seismic processes.

Writing – review & editing: Valentina Bruno, Mario Mattia, Fabrizio Pepe

Fluids significantly influence the deformation field through various physical and chemical processes (e.g., pore pressure variations, diffusive mass transfer, mineral precipitation, sub–critical crack growth, and phase transitions of water; Feng et al., 2023; Moore & Lockner, 2013; Sibson, 2000; Violay et al., 2015; Verberne et al., 2015). Such processes influence fault lubrication and modify the mechanical properties of rocks, such as shear strength and strain behavior (Bizzarri, 2012; Castelblanco et al., 2025; Cornelio et al., 2019). Fault lubrication diminishes the effective normal stress along fault planes, leading to a nearly complete stress drop, characterized by a very low residual friction coefficient. This process enhances fracture energy density and facilitates high slip velocities during seismic events (Bizzarri, 2012).

Laboratory experiments have successfully modeled the response of seismogenic structures undergoing lubrication processes (e.g., Verberne et al., 2020 and reference therein), and numerous studies have documented seismicity induced by anthropogenic fluid migration (e.g., Albaric et al., 2014; Evans et al., 2005; Stanchits et al., 2011), evidence from natural settings remains sparse. Specifically, the duration of deformation and the magnitude of seismic events triggered by fault activation in the presence of natural fluids are still poorly constrained, highlighting a critical gap in our understanding of fluid–fault interactions.

In this study, we investigate the deformation field characterizing the Peloritani Mts (northeastern Sicily) and the central and western sectors of the Aeolian Archipelago (southern Tyrrhenian Sea, Figures 1a and 1b) using position–time series GNSS and seismological data. We reconstruct the geometry and kinematics of tectonic structures and identify the depths at which seismic strain is released. Furthermore, we investigate the relationship between the activation of faults in the presence of fluids and velocities of displacement of blocks along fault planes to understand rupture propagation timing. Our findings suggest a fluid–mediated mechanism that promoted a deformation regime lasting 9 months, characterized by continuous low–magnitude seismic activity. This behavior deviates from conventional rupture propagation, which typically consists of a brief co–seismic phase dominated by a mainshock lasting only a few minutes, followed by a prolonged post–seismic phase characterized by low–magnitude seismicity and gradual stress relaxation. Finally, this study demonstrates that position–time series data from GNSS networks can reveal mesoscale tectonic deformation processes, even in regions lacking large–magnitude seismic events or significant ground displacement.

2. Geological Background

2.1. Regional Tectonic Setting

The tectonic evolution of northeastern Sicily and the Tyrrhenian Basin developed within the Neogene–Quaternary convergence between the Eurasian and African plates, primarily resulting in the westward and northwestward subduction of the Adriatic and Ionian lithospheres, respectively (Carminati & Doglioni, 2005; Carminati et al., 1998; Faccenna, Becker, et al., 2001).

Seismic tomography of the Tyrrhenian–Ionian subduction zone reveals positive P wave anomalies, interpreted as the descending Ionian lithosphere (Lucente et al., 1999). This pattern suggests slab breakoff beneath the southern Calabrian Arc (Maesano et al., 2017; Neri et al., 2009; Scarfì et al., 2018), and subvertical tears accommodating the slab's retreat and its southeastward propagation (Rosenbaum et al., 2008). Tear faults at the edges of the subducting lithosphere are known as Subduction Transform Edge Propagator (STEP, Govers & Wortel, 2005) and generally propagate perpendicularly to the subduction hinge (Nijholt & Govers, 2015).

The upper plate of the subduction system comprises three key structural domains moving from west to east: Vavilov (4.3–4.1 to 2.6 Ma) and Marsili (Late Pliocene to ∼1.87 Ma) back–arc basins (Carminati & Doglioni, 2005; Corradino et al., 2022; Faccenna, Funiciello, et al., 2001; Faccenna et al., 2007; Sartori, 1990), an arc–shaped volcanic ridge, represented by the Aeolian archipelago, and a forearc region including the Calabrian Arc and the Calabrian accretionary wedge (Corradino et al., 2020; Pepe et al., 2010; Figure 1a).

The Calabrian Arc is an allochthonous continental crust block known as the Calabria–Peloritani terrane (after Bonardi et al., 2001), which connects the southern Apennines with the Sicilian–Maghrebian chain (Figure 1a). In northeastern Sicily, the Calabrian Arc corresponds to the Calabro–Peloritan Nappe, which is constituted by imbricate sheets of Hercynian metamorphic rocks of the European paleo–margin and Meso–Cenozoic sedimentary covers (Ogniben, 1969). The Calabro–Peloritan Nappe overthrusts the Sicilian–Maghrebian chain, forming the backbone of the Peloritani Mts.

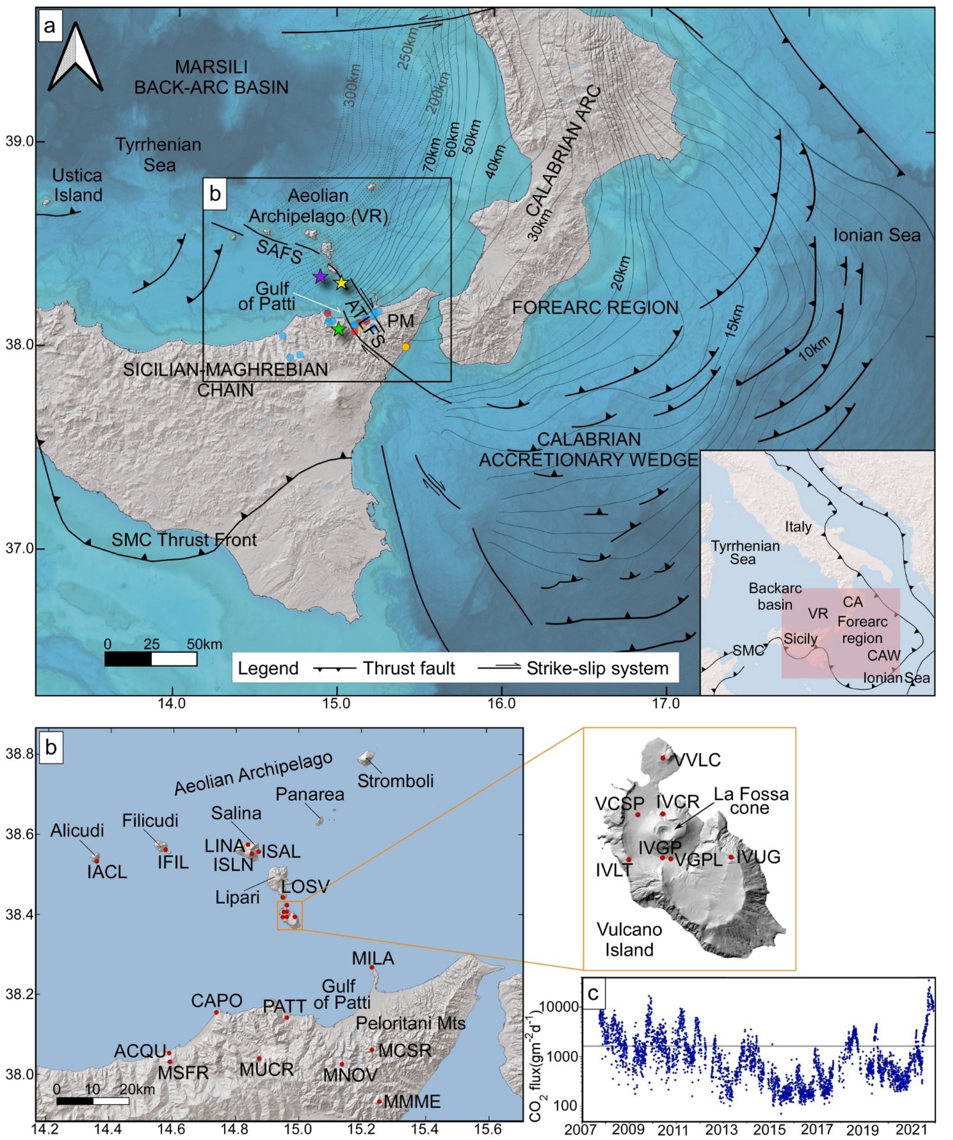

Figure 1. (a) Schematic tectonic map of the Tyrrhenian–Ionian subduction system (modified from Barreca et al., 2014, 2019; Billi et al., 2023). The light gray solid and dashed lines represent the depth contours of the slab model from Maesano et al. (2017). The depth contour interval is 1 km between 5 and 20 km depth, 5 km between 20 and 100 km depth, and 10 km from 100 km depth downward. Colored dots indicate the location of sampling sites for dissolved and bubbling gases (modified from Donato et al., 2021): red dots indicate gas samples from the mantle, yellow from the crust, and blue from the atmosphere. Stars represent the location of the three major earthquakes that occurred in 1,786 with Mw = 6.2 (green star), in 1978 with Mw = 6.1 (yellow star), and in 2010 with M_L 4.8 (violet star). Inset shows the location of the panel (a). Abbreviations: ATLFS, Aeolian Tindari–Letojanni Fault System; CA, Calabrian Arc; CAW, Calabrian accretionary wedge; PM, Peloritani Mts; SAFS, Sisifo–Alicudi Fault System; SMC, Sicilian–Maghrebian chain; VR, Volcanic ridge. (b) Location of the study area. Red dots indicate the location of the permanent GNSS stations used in this study. (c) Soil CO_2 diffuse degassing curve at the summit of La Fossa cone, Vulcano Island (modified from Inguaggiato et al., 2022).

The southern limit of the Calabrian Arc corresponds to the NW–SE trending right–lateral strike–slip Aeolian–Tindari–Letojanni Fault System (ATLFS, Figure 1a) located in northeastern Sicily. The fault system affects the area extending from the central Aeolian archipelago across the Gulf of Patti and the Peloritani Mts to the Ionian coast of eastern Sicily (Billi et al., 2006; Cultrera et al., 2017; Neri et al., 1996; Palano et al., 2012, 2015; Pondrelli et al., 2004) and the Ionian offshore (Barreca et al., 2019).

The earthquake distribution indicates that the deformation associated with the ATLFS activity is mainly confined to the northern and central sectors of the system (Barreca et al., 2014; Cultrera et al., 2017; Lo Mauro et al., 2025;

Scarfì et al., 2018). Here, deformation occurs through NW–SE trending, right–transtensional én–echelon fault segments, whose arrangement results in the formation of releasing stepover and pull–apart structures (Cultrera et al., 2017).

Most authors interpret the ATLFS as the upper plate expression of the STEP fault located on the southern edge of the Ionian slab (e.g., Govers & Wortel, 2005; Lo Mauro et al., 2025; Neri et al., 2012; Scarfì et al., 2016, 2018). However, alternative interpretations have also been proposed. Some researchers suggest that the ATLFS represents a discontinuity marking an area of incipient rifting (Dellong et al., 2018), while others consider it as part of an incipient oblique–extensional transfer zone, linking the active contractional belts in the Calabrian–Ionian region with those in the southern Tyrrhenian domain (Billi et al., 2006).

Another seismically active fault system is located in the southern Tyrrhenian Basin. Here, the shortening associated with the Eurasia–Africa convergence is accommodated by NE–SW trending én–echelon arranged thrust–faults and by a WNW–ESE trending strike–slip fault system extending from Ustica Island to the western portion of the Aeolian archipelago, between the Alicudi Island and the Lipari–Vulcano complex (Billi et al., 2007; De Astis et al., 2003; Favalli et al., 2005; Neri et al., 1996; Pondrelli et al., 2004; Scarfì et al., 2012, 2013). The WNW–ESE fault system is known in the literature as the Sisifo–Alicudi fault system (SAFS, Barreca et al., 2014, Figure 1a).

The central sector of the Aeolian archipelago (Lipari and Vulcano islands) is tectonically controlled by NW–SE oriented strike–slip faults and associated N–S to NE–SW extensional faults and fractures, forming pull–apart–type structures (Mazzuoli et al., 1995; Ventura, 1994). The NNW–SSE alignment of Lipari and Vulcano volcanoes has traditionally been interpreted as the northern expression of the ATLFS (e.g., Castro Melgar et al., 2021; De Ritis & Chiappini, 2023; Gioncada et al., 2003; Lanzafame & Bousquet, 1997; Mazzuoli et al., 1995; Neri et al., 1996; Palano et al., 2015; Pondrelli et al., 2004; Ventura, 1994). However, Barreca et al. (2014) propose that the current transpressive kinematics observed in the Lipari–Vulcano complex are linked to the eastward migration of the SAFS.

2.2. Seismological Setting

An analysis of seismicity over the past 40 years reveals a well–defined seismic belt characterized by high earthquake density, extending from Alicudi Island toward Salina, and continuing in a NW–SE direction into the Gulf of Patti and further inland into northeastern Sicily. This pattern closely follows the region's principal structural features, namely the Sisifo–Alicudi Fault System and the Aeolian–Tindari–Letojanni Fault System, which play a fundamental role in shaping the seismotectonic framework of the area and are spatially associated with several significant historical earthquakes.

Historical records document the occurrence of numerous damaging seismic events within this region. Among the most notable is the earthquake of 10 March 1786 (green star in Figure 1a), linked to the ATLFS, which reached a maximum intensity of IX on the MCS scale (estimated magnitude Mw ∼6.2; Rovida et al., 2022), causing widespread devastation across several villages facing the Gulf of Patti. More recently, on 15 April 1978, a Mw 6.1 earthquake struck approximately 10 km west of Capo Milazzo (yellow star in Figure 1a, Gasparini et al., 1982, 1985; Rovida et al., 2022). The event produced its most severe effects along the Tyrrhenian coast of northeastern Sicily and was widely felt across much of Sicily and Calabria. Significant structural damage and building collapses have been reported in nearly 100 localities along the Gulf of Patti and in the Aeolian Islands (Barbano et al., 1979).

Further confirmation of the area's seismic potential came in August 2010 when an M_L 4.8 earthquake struck approximately 9 km southwest of Vulcano Island (violet star in Figure 1a, Alparone et al., 2023). Although moderate in magnitude, the event was widely felt across north–eastern Sicily and caused minor but significant damage to several masonry structures (Azzaro et al., 2014).

2.3. Surface Gas Release

North–eastern Sicily and the central sector of the Aeolian Archipelago exhibit extensive degassing activity, including geothermal springs, fumaroles, gas vents, bubbling pools, and diffuse soil degassing. These manifestations are spatially organized along NNW–SSE trending structural lineaments linked to the ATLFS (Decrée et al., 2005; Donato et al., 2021; Giammanco et al., 2008; Inguaggiato et al., 2022; Italiano & Caruso, 2011).

In the Peloritani Mts area, the dominant gas emissions typically linked to hydrothermal activity exhibit mantle–derived provenance (colored dots in Figure 1a), as demonstrated by elevated $^3He/^4He$ ratios (Donato et al., 2021; Giammanco et al., 2008). Analyses of both the surface efflux of mantle–derived gases and the P–T conditions of fluids suggest a pressurized gas source at a depth of 7–12 km, corresponding to the range of hypocentral depths of seismic swarms (Giammanco et al., 2008).

Along the central sector of the Aeolian Archipelago, degassing activity was documented at the volcanic islands of Vulcano, Lipari and Salina. Vulcano Island was affected by sustained degassing activity, periodically interrupted by degassing crises occurring in 1978–1980 (Carapezza et al., 1981), 1988–1991 (Cioni & D'Amore, 1984; Chiodini et al., 1992), 1996 (Capasso et al., 1999), 2004–2007 (Cannata et al., 2012; Capasso et al., 2014; Diliberto, 2017), 2009–2010 (Inguaggiato, Calderone, et al., 2012; Vita et al., 2012), and 2021 (Federico et al., 2023). These crises consisted of an increase in volatiles (i.e., SO_2, CO_2, and H_2O fluxes) and energy output (Inguaggiato, Mazot, et al., 2012). In particular, soil CO_2 emission at the summit of the La Fossa cone is represented by a curve with a general decreasing trend from 2007 to 2015, followed by a positive trend since 2016, marked by a series of increasing peaks in 2016, 2017,2018, and 2021 (Figure 1c, Inguaggiato et al., 2022). The last peak, corresponding to the highest value of CO_2 emission, occurred when Vulcano experienced a period of unrest, and most of the parameters continuously monitored by the INGV surveillance network showed stunning variations, in some cases by orders of magnitude over background levels (Aiuppa et al., 2022; Di Traglia et al., 2023; Diliberto et al., 2024; Federico et al., 2023).

Hot springs and fumaroles have also been documented on Lipari Island (De Ritis et al., 2013). Hydrothermal activity is concentrated along N–S trending faults and fractures and is located in the western sector of the island (Di Luccio et al., 2021; Forni et al., 2013; Ventura et al., 1999).

The geochemical prospection of the fluids circulating over the Salina Island highlighted the existence of reservoirs of both fresh and thermal water, whose submarine expression is represented by persistent gas bubbling. The released gases are CO_2–dominated and marked by a helium isotope ratio consistent with the magmatic origin of the gas phase (Italiano & Caruso, 2011 and references therein).

3. Materials and Methods

3.1. GNSS Data

The GNSS data were collected from 22 permanent stations located in the western and central islands of the Aeolian Archipelago (Alicudi, Filicudi, Salina, Lipari and Vulcano islands) and the Peloritani Mts area (Figure 1b) between 1999 and 2023. These stations are part of the monitoring networks managed by the Osservatorio Etneo of the Istituto Nazionale di Geofisica e Vulcanologia (INGV–OE), the Rete Integrata Nazionale GPS (RING) network managed by the INGV (http://ring.gm.ingv.it/), the ItalPOS network (https://hxgnsmartnet.com/) and the NetGEO network (http://www.netgeo.it/).

GNSS data processing was carried out with the GAMIT/GLOBK software package version 10.71 (Herring et al., 2015, 2018a, 2018b) developed at the Harvard Smithsonian Center of Astrophysics, Massachusetts Institute of Technology (MIT), and the Scripps Institution of Oceanography, University of California, San Diego. Furthermore, data from 14 IGS stations (BOR1, CAGL, GLSV, GRAS, GRAZ, LROC, MATE, NOT1, NOTO, POTS, VILL, WSRT, WTZR, ZIMM) and the station EIIV installed in Catania by the INGV were processed to constrain the solutions. The GAMIT module was used to estimate coordinates, variance–covariance matrices, atmospheric delays, ambiguities and orbital parameters, and derive weakly constrained daily solutions. The solution was iterated automatically three times by applying a weighted least–squares algorithm to minimize the residuals between the estimated coordinates and the a priori ones. The linear combination of phase and code Melbourne–Webbena wide–lane was used to resolve ambiguities. Satellite orbits were fixed using IGS final orbits and a second—order ionospheric correction was applied using IGS final ionospheric products (https://igs.org/products/). The tropospheric delay was estimated using the Vienna Mapping Function (VMF1) (Boehm et al., 2006) by setting a cutoff angle of 10°, and the ocean tidal load was estimated through the Finite Element Solution (FES2004) model (Lyard et al., 2006). The International Earth Rotation Service (IERS) 2003 model was used for diurnal and semidiurnal solid Earth tides, and the Earth Orientation Parameters (EOP) were constrained with a priori parameters obtained from IERS Bulletin B.

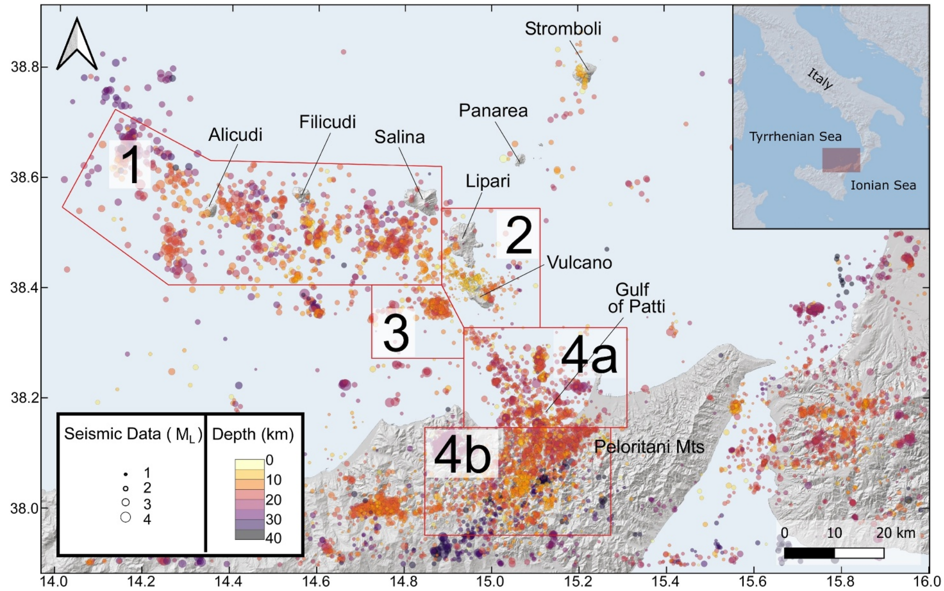

Figure 2. Map of the area showing the locations of seismic events. Red polygons indicate the five areas where seismic strain release was calculated.

The weakly constrained solutions were aligned with the IGB14 reference frame and rotated into the Nubia–fixed reference frame (Altamimi et al., 2017) using GLOBK's GLORG module. The daily positions of each component (North, East, and Up) were corrected using the interactive Matlab®–based Tsview software (Herring, 2003), which can identify and estimate offsets associated with instrumental changes. The identification of outliers and estimation of annual, semi–annual, and noise components were performed using the Hector software, which is based on maximum likelihood estimation (MLE) (Bos et al., 2013; Bos & Fernandes, 2021). Outliers were removed from the time series based on the interquartile range (IQR) of the residuals from the linear least squares fit. We set an IQ factor of 2, and residuals exceeding the chosen threshold (IQR multiplied by this factor) were classified as outliers. To obtain a realistic estimate of the uncertainty, we used a combination of white noise and a generalized Gauss–Markov noise model (Kall et al., 2019).

The GNSS data processing allowed us to generate the position–time series of the horizontal and vertical components (North, East, and Up) for each station from 1999 to 2023. This work presents the position–time series from 2011 because significant deformations have been observed since that year.

The GNSS velocity field was computed in the Nubia–fixed reference frame for the period 1999–2023 using position–time series from stations that collected data for at least 2.5 years.

The GNSS data were also used to investigate surface deformations (i.e., deflation and inflation) on Vulcano Island. We determined the areal variation of a triangle formed by the three GNSS stations IVLT–IVCR–IVUG, which includes the La Fossa cone, from 2011 to 2023. The area of the triangle was calculated using Heron's formula, with the side lengths derived from the 3D coordinates (North, East, Up) of each station located at the triangle's vertices.

3.2. Seismic Data

Seismological data were selected from the database of the Istituto Nazionale di Geofisica e Vulcanologia (Alparone et al., 2023; Barberi et al., 2020; https://www.ingv.it/risorse-e-servizi/archivi-e-banche-dati), focusing on shallow crustal seismicity ≤40 km depth within the study area outlined in Figure 2 for the time interval 2011–2023. A data set of 9,000 hypocenters was relocated using the tomoDDPS double–difference algorithm (Zhang et al., 2009) and a 3D velocity model derived by the integration of passive and active seismic data (the last acquired during the "TOMO–ETNA experiment," FP7 "MED–SUV," Barberi et al., 2018), to improve accuracy in hypocenter localization. The algorithm has the advantage of using a combination of both absolute and differential arrival–time readings between couples of close–spaced earthquakes, which have the same velocity profile along the ray–path

10.1029/2025GC012446

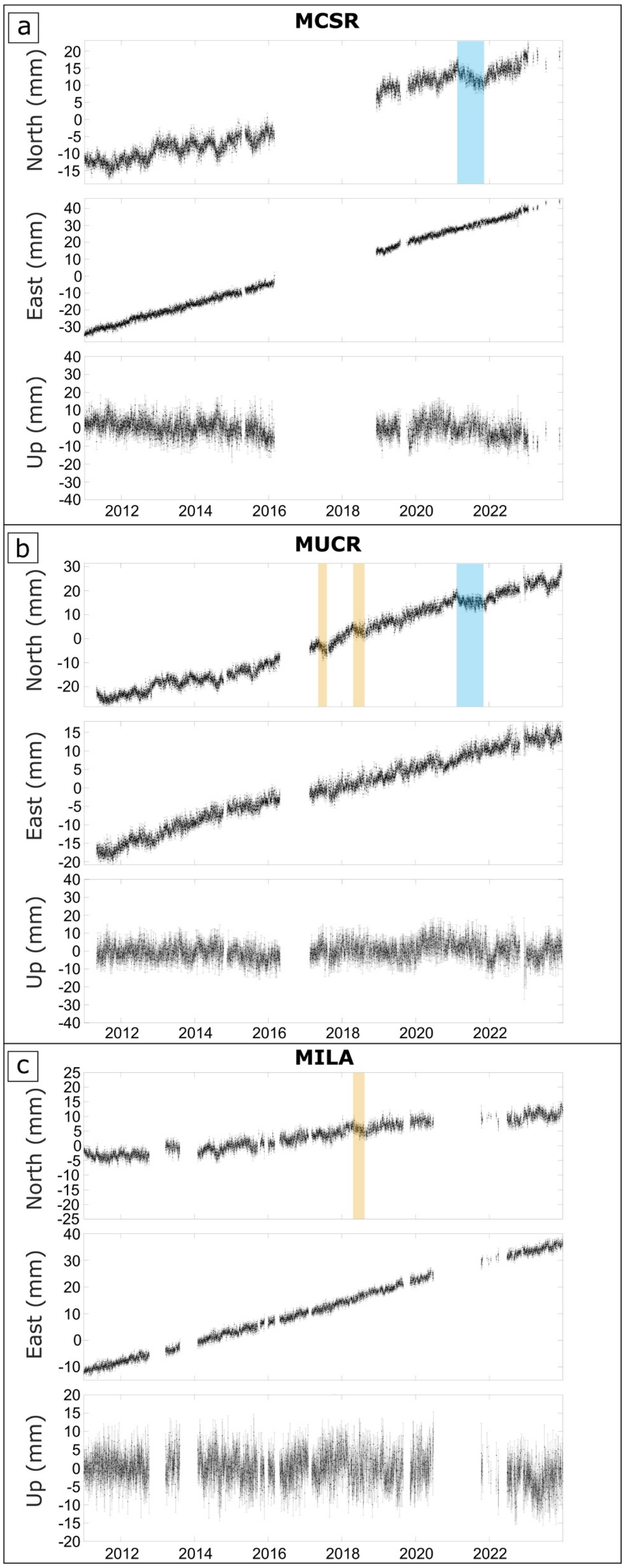

Figure 3.

between the source and a common receiver. Since the spatial and velocity paths are almost identical, the difference in arrival times is reasonably attributed only to the spatial offset between the seismic events. The algorithm was able to localize earthquakes with horizontal and vertical uncertainties of approximately 0.12 ± 0.05 km and 0.17 ± 0.08, respectively, and with an average root–mean–square travel–time residual of 0.03 s.

We quantified seismic activity by calculating the cumulative seismic strain curves, which are indicative of seismicity within key volumes. To define these volumes, we first looked at the depths of the earthquake foci. Since changes in the depth distribution occur around 3, 8, 13, and 20 km (Figure S1 in Supporting Information S1), we divided the depth into five intervals: 0–3 km, 3–8 km, 8–13 km, 13–20 km, and 20–40 km.

To define the horizontal boundaries of each area, we used seismic energy release maps. These maps were built on a 3 km grid, with the same five depth intervals and four time periods: 2016–2017, 2017–2018, 2020–2021, and 2021–2022 (Figure S2 in Supporting Information S1). Based on the location of the strongest energy release at different depths, we identified five main zones, labeled 1, 2, 3, 4a, and 4b (Figure 2).

Combining the five depth intervals with the five horizontal zones gave us 25 key volumes. These volumes capture most of the seismic activity in the study area.

Finally, the seismic strain release curves were computed using Richter's relationship for seismic energy (E in erg), that is $\log(E) = 9.9 + 1.9\, M_L - 0.024\, M_L^2$.

4. Results

We analyzed (a) GNSS data to obtain position–time series of GNSS stations and the velocity field and (b) seismic data to identify areas and depths where seismic strain is released. These analyses enable us to identify deformation zones within the study area and comprehend the kinematics of the major tectonic structures.

4.1. GNSS Position–Time Series

The GNSS position–time series from stations in the Peloritani Mts area and the Aeolian Archipelago exhibit significant trend variations from 2011 to 2023. We define a significant trend variation as a rapid excursion in a trend that is preceded and followed by a long–term trend. This criterion distinguishes these events from variations that exhibit an oscillatory character consistent with seasonal effects. We focus on data from stations with high temporal continuity and low noise, ensuring reliable results.

Stations in the Peloritani Mts area exhibit notable variations in the north component. Significant changes were observed at the MUCR station in 2017 (Figure 3b), at both the MUCR and MILA stations in 2018 (Figures 3b and 3c), and at the MUCR and MCSR stations in 2021 (Figures 3a and 3b).

Figure 3. GNSS position–time series of the three components from GNSS stations located in the Peloritani Mts area: (a) MCSR station, (b) MUCR station, (c) MILA station. See Figure 1b for the stations' location. One–sigma error bars are included for all data points. Blue bands mark significant trend variations that occurred in 2021. Yellow bands mark other significant trend variations to a lesser extent than those in 2021.

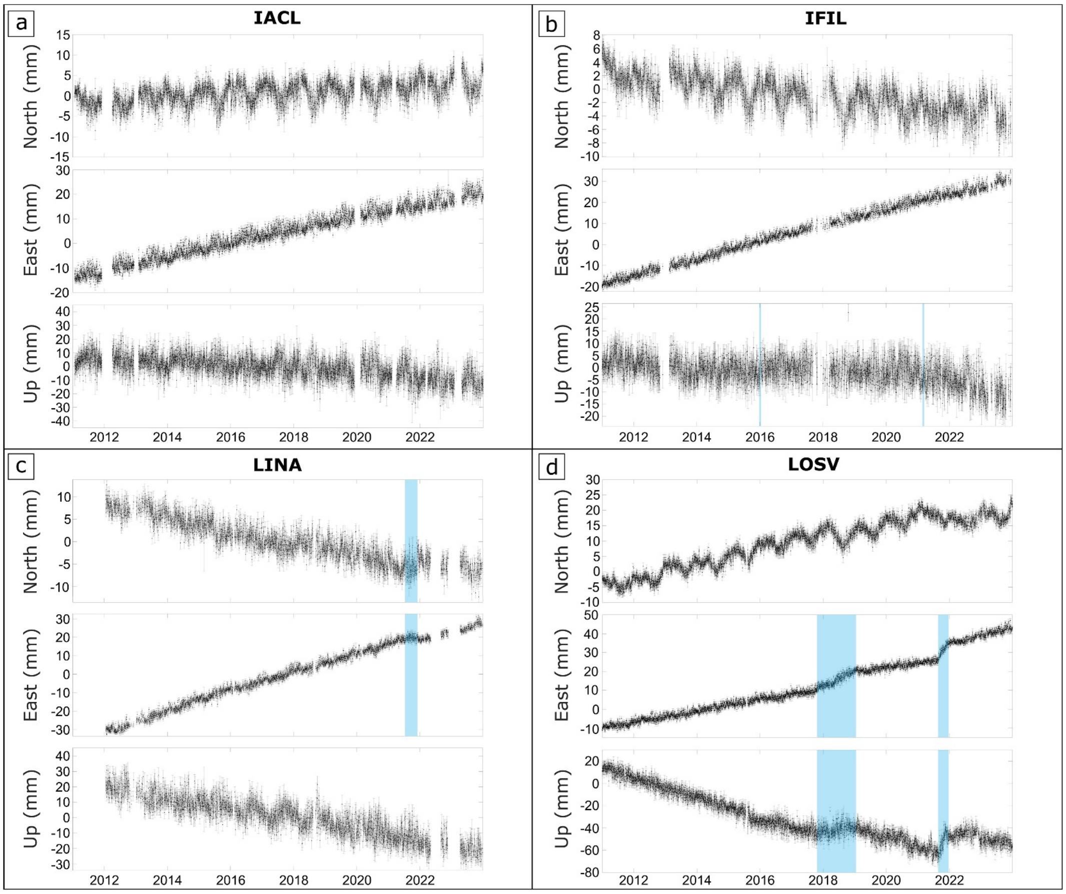

Figure 4. GNSS position–time series of the three components from GNSS stations located in the Aeolian archipelago: (a) IACL station at Alicudi Island; (b) IFIL station at Filicudi Island; (c) LINA station at Salina Island; and (d) LOSV at Lipari Island. See Figure 1b for the stations' location. One–sigma error bars are included for all data points. The vertical blue lines highlight trend variations.

Specifically, we observed a notable southward displacement at the MUCR station from May to August 2017 (Figure 3b). A southward displacement was also recorded at the MUCR and MILA stations between April and August 2018 (Figures 3b and 3c). The most prolonged southward displacement was measured at the MCSR and MUCR stations from February to December 2021, as illustrated in Figures 3a and 3b.

GNSS position–time series from the western Aeolian Archipelago (Alicudi and Filicudi islands) display linear displacement trends in the horizontal and vertical components (Figures 4a and 4b). An exception occurs for the vertical component of the Filicudi station, which exhibits two distinct trend changes in December 2015 and February 2021 (Figure 4b). In contrast, stations on the Salina and Lipari islands exhibit trend variations in the north and east components in 2021 and the east and up components in 2018 and 2021, respectively (Figures 4c and 4d). These variations indicate a shift in the Salina station's motion from a south–east direction before 2021 to a northwest direction during 2021. Similarly, the Lipari station's northeastern motion accelerated eastward, accompanied by uplift events in 2018 and 2021.

On Vulcano Island, the IVCR–IVLT–IVUG areal variation indicates a transition from a period of deflation at the La Fossa cone, observed between 2011 and 2017, to a phase of inflation starting in February 2017 (Figure 5). Furthermore, the inflation rate increases from February to August 2017, from March to August 2018, from April to August 2019, and notably from September to November 2021 (Figure 5). The last event was particularly significant, marked by a sharp increase in the areal variation of about 17 parts per million (ppm) during 2021.

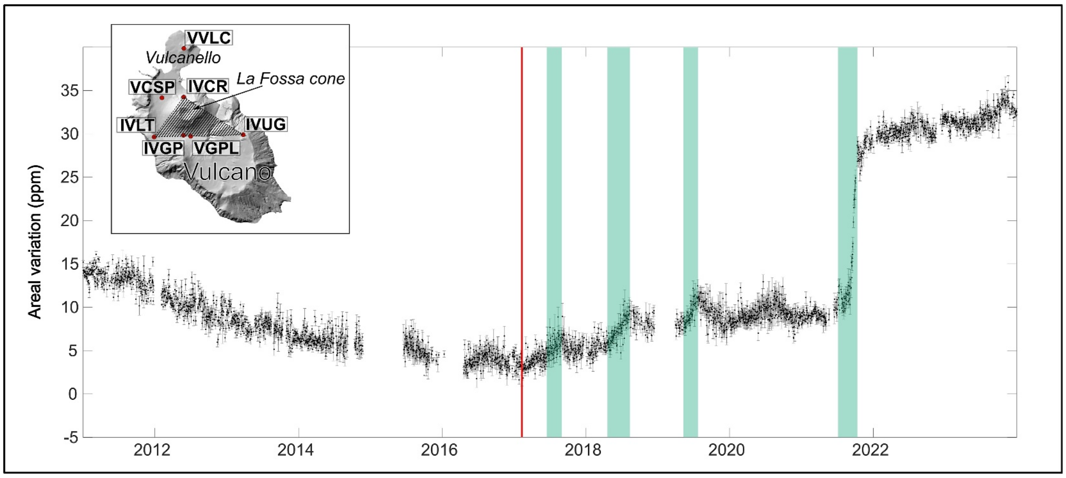

Figure 5. Areal variation of the triangle with vertices on the GNSS stations IVLT, IVCR, and IVUG at Vulcano Island. One–sigma error bars are included for all data points. Positive trends indicate the areal expansion, associated with the inflation process, while negative trends indicate the areal contraction associated with the deflation process. The red line marks the transition from deflation to inflation at the La Fossa cone. Green bands indicate rapid increases in the inflation rate. The inset shows the stations' localization.

4.2. GNSS Velocity Field

The horizontal velocity field, referenced to the Nubian frame, shows that velocity vectors vary significantly in both magnitude and orientation across the study area from 1999 to 2023 (Figure 6), delineating four primary deformation zones: (a) between Alicudi and Filicudi islands; (b) between Filicudi and Salina islands; (c) between Salina and Lipari islands; and (d) in the Peloritani Mts area, specifically between the sectors west and east of the Tindari–Letojanni line.

Vector analysis reveals that the Filicudi station moves southeastward (~N130°) at a rate of 1.5 ± 0.7 mm/yr relative to the fixed Alicudi station (Figure 6b). Similarly, the mean vector from Salina stations moves southeastward (~N110°) at a rate of 1.2 ± 0.6 mm/yr relative to the fixed Filicudi station (Figure 6c). Additionally, the difference between the Lipari station's vector and the mean vector from Salina stations indicates that Salina moves southeastward (~N155°) at a rate of 3.3 ± 0.6 mm/yr relative to the fixed Lipari station (Figure 6d). These findings suggest the presence of three right–lateral strike–slip fault zones between the four islands.

In the Peloritani Mts area, the stations west of the Tindari–Letojanni line (MSFR, ACQU, CAPO, MUCR, PATT, and MNOV, Figure 6a) exhibit an average velocity of 3.9 ± 0.2 mm/yr with a northeast orientation (~N40°). In contrast, the stations east of this line (MILA, MMCSR, and MMME, Figure 6a) display a higher average velocity of 5.0 ± 0.2 mm/yr with an east–northeastward orientation (~N70°). The mean velocity difference between these two groups indicates that the eastern sector moves southeastward (~N125°E) at a rate of 2.6 ± 0.4 mm/yr (Figure 6e). This finding confirms the presence of a right–lateral strike–slip fault zone along the Tindari–Letojanni line.

4.3. Seismic Activity: Magnitude and Seismic Strain Release

The analysis of seismic activity from 2011 to 2023 enabled the identification of areas with the highest density of seismic events using hypocentral location data (Figure 2). The temporal evolution of seismicity in the five investigated areas is shown in Figure S3 in Supporting Information S1. Seismic activity is mainly concentrated in Area 1, dominated by events with magnitudes (M_L) between 1.5 and 2.5 (Figure S3a in Supporting Information S1), and in Areas 4a and 4b, where magnitudes predominantly range between 0.5 and 1.5 (Figures S3d and S3e in Supporting Information S1, respectively). In contrast, Areas 2 and 3 exhibit lower seismic event frequency compared to the others, mainly with magnitudes between 0.5 and 1.5 (Figures S3b and S3c in Supporting Information S1, respectively).

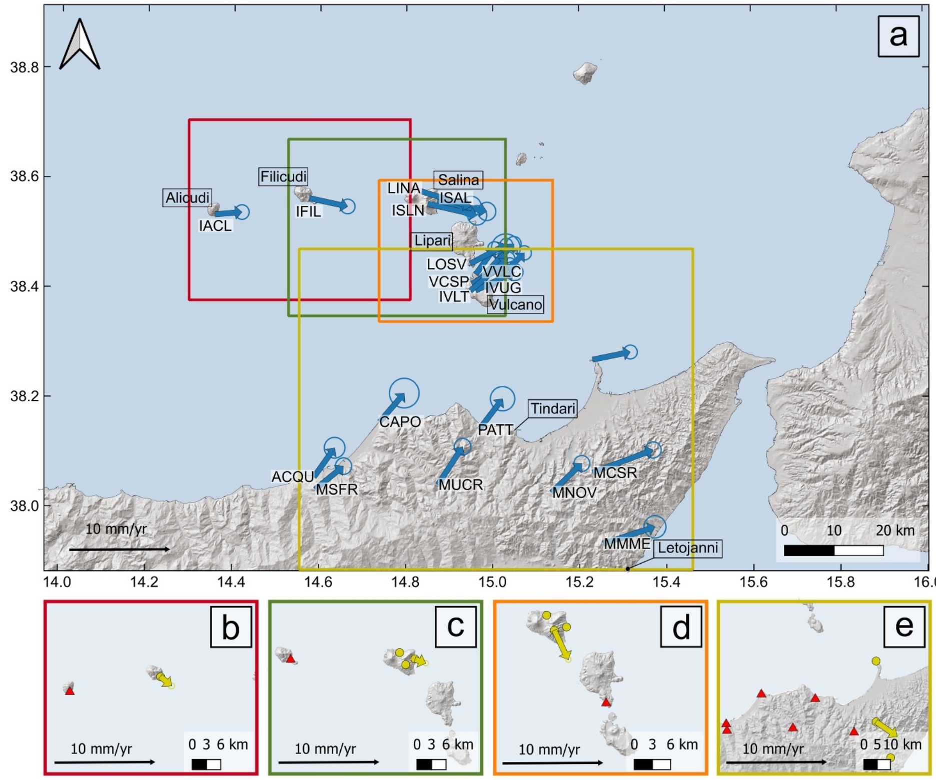

Figure 6. GNSS horizontal velocities and relative velocities across the primary deformation zones. (a) Horizontal velocities in the Nubia–fixed reference frame, shown with 95% confidence ellipses. The colored rectangles outline the four zones detailed in the boxes (b–e). (b–e) Velocity vectors (yellow arrow) of selected stations (yellow circles) computed relative to fixed ones (red triangles): (b) Alicudi–Filicudi, (c) Filicudi–Salina, (d) Salina–Lipari, and (e) the Peloritani Mts area.

During the entire observation period, the maximum recorded magnitude was 4.6 in Area 2. Within this framework, the year 2021 was selected for a more detailed analysis because it was characterized by (a) significant variations in the trends of position time series, in both the Peloritani Mts area and the Aeolian Archipelago (see Section 4.1) and (b) a distinct increase in seismic event frequency in Areas 3 and 4a (Figures S3c and S3d in Supporting Information S1). This seismic activity featured magnitudes ranging from 0.5 to 1.5 in Area 3 (beginning in late 2021) and from 0.5 to 2.5 in Area 4a (during the first half of 2021). The graphs in Figure 7 illustrate the seismic strain release values for each depth interval over time in the respective area (see Section 3.2 for area identification methodology). Notably, the curves exhibit pronounced jumps along their trends, corresponding to rapid increases in seismic strain release. Specifically, Area 1, encompassing the Alicudi, Filicudi, and Salina islands, exhibits predominant strain release within the 8–13 km (light blue curve in Figure 7b) and 13–20 km (purple curve in Figure 7b) depth ranges, with numerous increases over time.

Area 2, located southwest of Vulcano Island, is predominantly characterized by strain release at depths of 8–13 km (light blue curve in Figure 7c). In contrast, Area 3, encompassing Lipari and Vulcano islands, exhibits a relatively subdued strain release compared to other areas, with notable contributions from the 3–8 km (green curve in Figure 7d) and 8–13 km (light blue curve in Figure 7d) depth ranges.

Finally, in Area 4a (the Gulf of Patti), the highest energy release occurs at depths of 8–13 km and 13–20 km (light blue and purple curves in Figure 7e), whereas in the Peloritani sector (Area 4b), it is predominantly concentrated at depths greater than 13 km (purple and blue curves in Figure 7f).

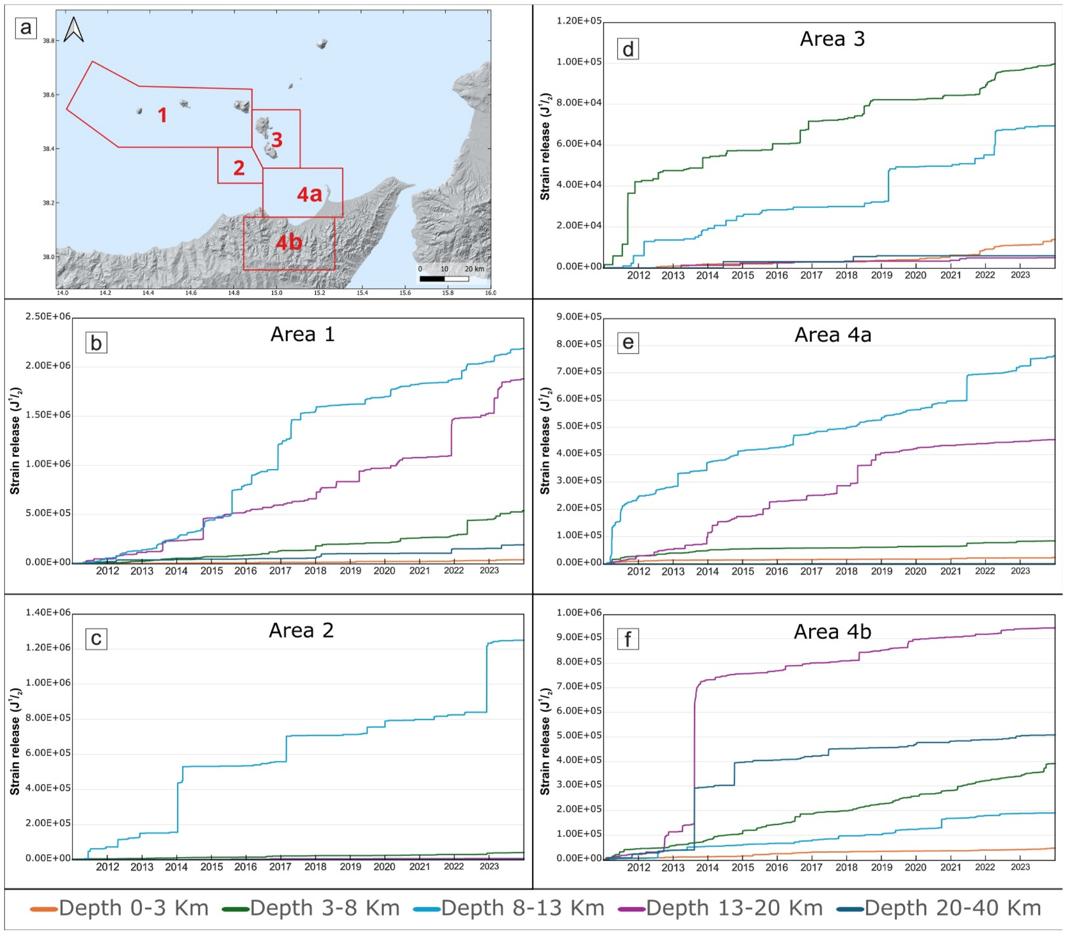

Figure 7. Cumulative seismic strain release curves calculated for the five key areas (described in paragraph Section 3.2). (a) Shows the map highlighting these five areas, bordered by red polygons where the seismic strain release was calculated. (b–f) Shows the seismic strain release curves calculated for five depth levels for each area. *Y*–axis scale, representing strain release in ($J^{1/2}$), differs between the subplots according to the strain release values. Legend indicates the colors corresponding to the depth intervals for which the seismic strain release curves are plotted.

5. Discussions

5.1. Structural Framework of the Area Between the Peloritani Mts and the Aeolian Archipelago

The analysis of the GNSS velocity field reveals four main right–lateral strike–slip fault zones critical for accommodating deformation in the Peloritani Mts area and the western and central sectors of the Aeolian Archipelago (Figures 6b and 6e, see Section 4.2). The fault systems are located: (a) between Alicudi and Filicudi islands; (b) between Filicudi and Salina islands; (c) between Salina Island and Lipari Island; and (d) between the sectors west and east of the Tindari–Letojanni line. The four deformation zones are displayed as shaded green bands in Figure 8a.

To determine the orientation of these strike–slip fault systems, we analyzed the focal mechanisms proposed by Scarfì et al. (2016) within the study area (Figure 8a). Additionally, we utilized the orientation diagram of the principal strain axes responsible for forming the Principal Displacement Zone (PDZ) based on the Riedel shear model. The diagram for the Peloritani Mts area is illustrated in Figure 8b. This approach allowed us to integrate GNSS data with theoretical models of shear deformation, providing a comprehensive understanding of the fault system's geometry and kinematics.

In the southern sector of the study area, the PDZ's orientation was determined through an analysis of fault planes from extensional focal mechanisms and the direction of conjugate strike–slip faults. The results indicate that the

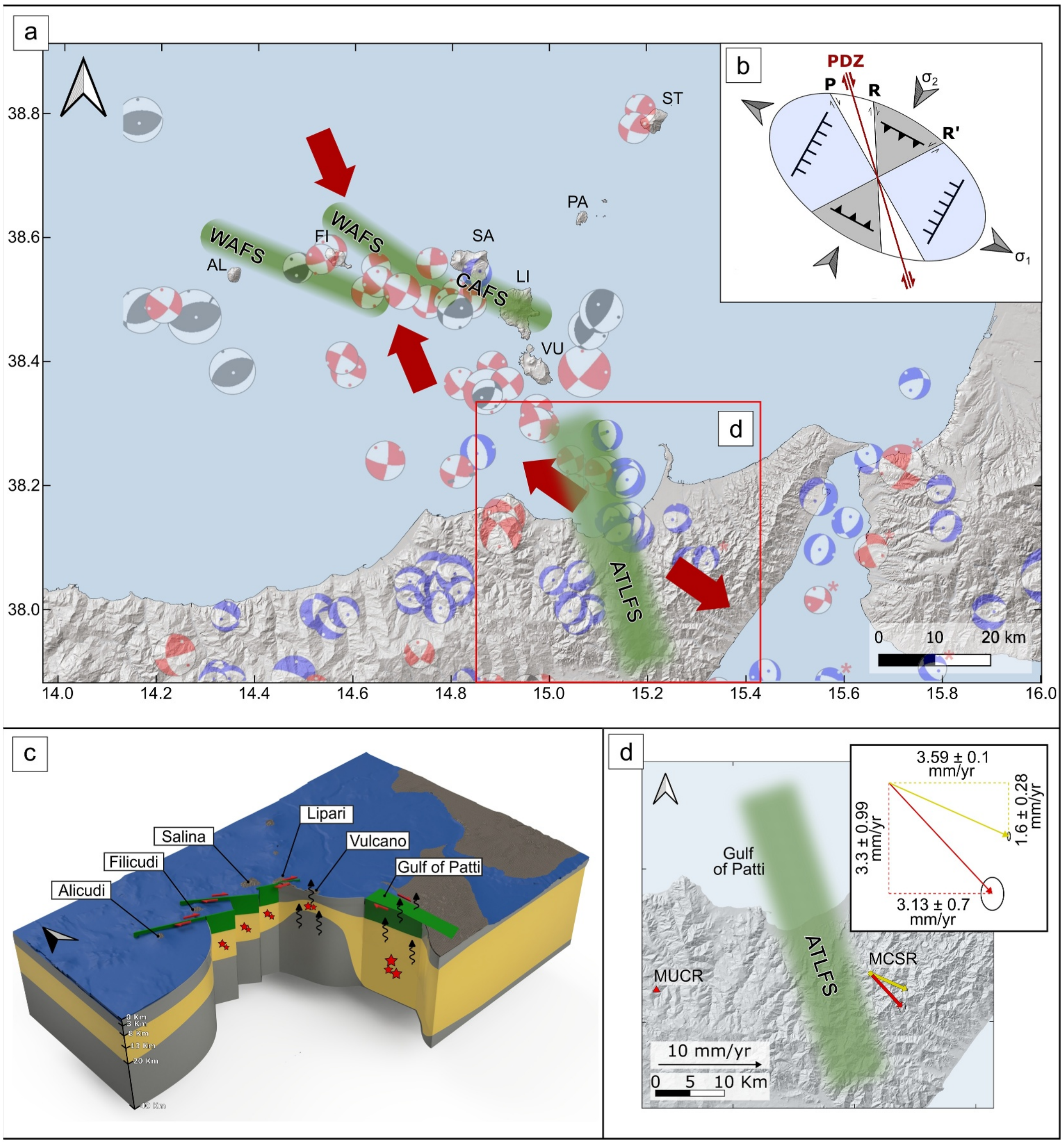

Figure 8. (a) Sketch map of the study area showing the four main right–lateral strike–slip fault zones (green bands). Focal mechanisms derive from Scarfì et al. (2016). Red arrows indicate the inferred kinematic framework Abbreviations: AL, Alicudi; ATLFS, Aeolian Tindari–Letojanni Fault System; CAFS, Central Aeolian Fault System; FI, Filicudi; LI, Lipari; PA, Panarea; SA, Salina; ST, Stromboli; VU, Vulcano; WAFS, Western Aeolian Fault System. (b) Orientation diagram of the principal strain axes responsible for the formation of the Principal Displacement Zone (PDZ) in the Peloritani Mts area, interpreted using the Riedel shear model and the fault plane orientation derived from focal mechanism data. (c) 3D view of the study area extending to a depth of 40 km, showing the four right–lateral strike–slip fault zones (green polygons) and seismogenic layers (yellow layer). Red stars indicate locations within the seismogenic layer characterized by significant seismic strain release. Wavy black arrows mark sites of surface gas emissions. (d) Velocity vectors of the MCSR station (yellow circles) for the period before 2021 (yellow vector) and for the year 2021 (red vector), computed relative to the local fixed station MUCR (red triangle). The inset displays the east and north velocity components for both periods, along with the resultant vectors: before 2021 (yellow vector) and during 2021 (red vector). Black ellipses represent one–sigma confidence.

PDZ exhibits an NNW–SSE orientation characterized by right–lateral transtensional kinematics (Figure 8b). This deformation pattern aligns well with the southern part of the strain accumulation zone, known in the literature as the ATLFS (Cultrera et al., 2017; Faccenna et al., 2011; Goes et al., 2004). Cultrera et al. (2017) documented that the offshore extension of the Tindari–Letojanni fault system is represented by an active releasing zone located in the Gulf of Patti. The earthquake map presented in this study confirms the presence of a deformation zone encompassing both the Peloritani Mts area and the Gulf of Patti. In the western and central sectors of the Aeolian

Archipelago, the orientation of the PDZs ranged from WNW–ESE to NW–SE. This orientation is derived from an analysis of fault plane directions associated with compressional focal mechanisms and the directions of conjugate strike–slip faults.

Within the context of the current geodynamics of the central Mediterranean, the ATLFS accommodates upper plate deformation resulting from lithospheric tearing at the slab edge along the southern margin of the Calabrian Arc (Barreca et al., 2016 and reference therein). This process is responsible for forming a STEP fault, as described by Govers and Wortel (2005). In contrast, the PDZs located between Alicudi and Filicudi islands, and between Filicudi and Salina islands, here referred to as the Western Aeolian Fault System (WAFS), are interpreted as lateral ramps where displacement is transferred from one thrust fault segment to another laterally. Specifically, these lateral ramps connect independent crustal tectonic blocks representing segments of the tectonic boundary between Africa and Eurasia, and are involved in the ongoing convergence process (Billi et al., 2023).

The seismogenic layer reaching depths of up to 40 km in the ATLFS (Figures 7e and 7f) supports its interpretation as a crustal–scale deformation zone, indicating the involvement of the entire crust in seismic activity (Figure 8c). Conversely, the layers primarily ranging from 8 to 20 km in depth in the WAFS (Figure 7b) suggest that these structures are confined to a smaller, crustal–thrust fault system (Figure 8c).

Goes et al. (2004) have suggested that the PDZ identified in the central Aeolian sector, between the Lipari and Salina islands, might represent the northern sector of the ATLFS. However, based on its kinematics derived from the geodetic data of this study, the segment of the PDZ zone between Lipari and Salina islands could either represent a lateral ramp similar to those observed in the WAFS or constitute the northern extension of the ATLFS.

5.2. Relationship Between Fluid Circulation and Volcanic Activity

The analysis of the areal variation on Vulcano Island indicates that the La Fossa cone transitioned from a deflation phase to an inflation phase in February 2017, which persisted until 2023, marking the conclusion of the study period. This inflation phase was marked by several rapid inflation events, with the most significant occurring at the end of 2021. The latter event can be well placed within the context of the volcanic unrest observed that year, which was characterized by significant variation in degassing, seismicity and ground deformation as widely documented in the literature (Aiuppa et al., 2022; Di Traglia et al., 2023; Diliberto et al., 2024; Federico et al., 2023). Furthermore, increases in inflation rates observed between February and August 2017, March and August 2018, April and August 2019, and notably in 2021 (as evident in the peaks of areal variation, Figure 9a) temporally correlate with periods of enhanced CO_2 diffuse degassing at Vulcano Island (reflected in the peaks of CO_2 flux emission, Figure 9b). This correlation suggests that increased fluid circulation played a significant role in the inflation of the volcano.

5.3. Relationship Between Fluid Circulation and Fault Activity

The position–time series of GNSS from the MUCR and MCSR stations in the Peloritani Mts area (Figures 5a and 5b) show significant northward velocity variations, with the most prolonged and pronounced variation during 2021. GNSS–derived velocity analysis reveals that the eastern sector of the GPTLFS experienced an increase in southward velocity, from 1.6 ± 0.28 mm/year before 2021 to 3.3 ± 0.99 mm/year during 2021, relative to the fixed station MUCR reference station located west of the ATLFS (Figure 8d). In contrast, the eastward velocity component exhibited a minor decrease, from 3.59 ± 0.1 mm/yr before 2021 to 3.13 ± 0.7 mm/yr in 2021, which is not statistically significant (Figure 8d). These findings highlight a significant southward acceleration of the eastern block of the ATLFS during 2021.

The deformation process, captured in GNSS time series from stations in the Peloritani Mts area, was accompanied by a rapid seismic strain release at depths between 8 and 13 km in the offshore region of the ATLFS, as reflected by a significant jump in the strain release curve during 2021 (area 4a in Figure 7e).

It is essential to note that a temporal correlation exists between two significant events: (a) the acceleration of the eastern sector of the ATLFS relative to the western sector in 2021, which was accompanied by increased seismic strain release (evidenced by the jumps in the curves in Figure 7e), and (b) the significant rapid inflation event observed at Vulcano in 2021 (Figure 4), linked to heightened CO_2 emissions on Vulcano Island (see Section 5.2). This temporal correlation suggests that fluid circulation, manifested as gas emissions in the Peloritani Mts area

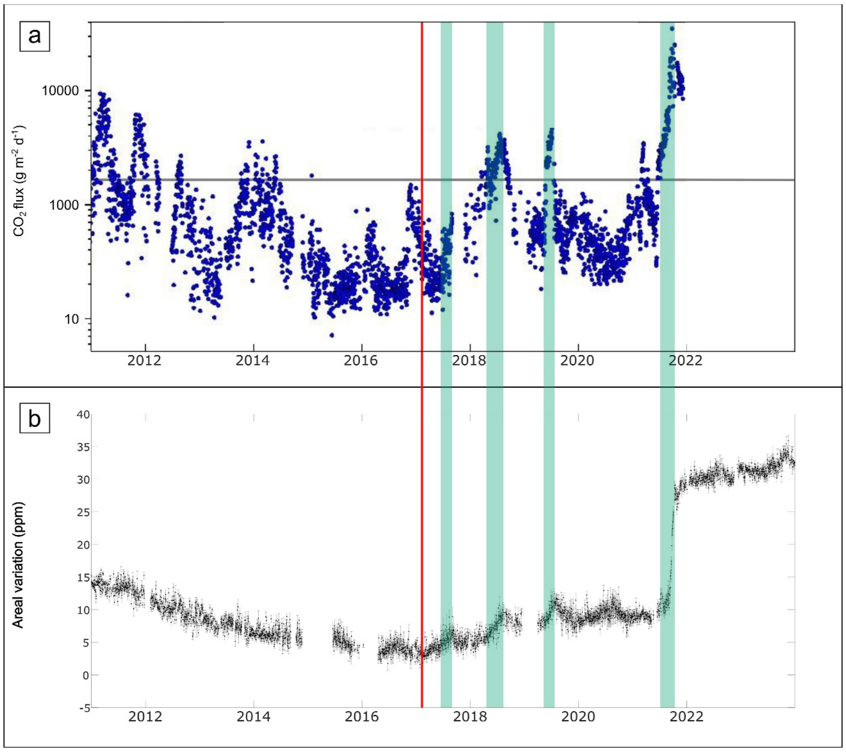

Figure 9. Comparison between the areal variation associated with the inflation/deflection processes at Vulcano Island and soil CO_2 degassing. (a) Daily average of soil CO_2 diffuse degassing curve at the summit of the La Fossa cone. Gray horizontal line indicates the mean value of 1,637 g m^{-2} d^{-1} (modified from Inguaggiato et al., 2022). (b) Areal variation of the triangle with vertices on the GNSS stations IVLT, IVCR, and IVUG at Vulcano Island (see Figure 5 for station location). One–sigma error bars are included for all data points. Positive trends indicate the areal expansion, associated with the inflation process, whereas negative trends indicate the areal contraction associated with the deflation process. The red line marks the transition from deflation to inflation at the La Fossa cone within Vulcano Island. Green bands highlight periods of rapid inflation rate increases, which coincide with increases in CO_2 flux (graph below).

(Donato et al., 2021, and references therein), may be intensified and play a pivotal role in increasing the velocities of upper–crust block displacement along the ATLFS.

The influence of fluids on fault activity occurs through physical and chemical processes (e.g., pore pressure variations, diffusive mass transfer, mineral precipitation, sub–critical crack growth, and phase transitions of water), which are known to reduce the effective normal stress along fault planes, thereby facilitating fault slip and triggering seismicity (e.g., Benson et al., 2020; Bizzarri, 2012; Castelblanco et al., 2025; Cornelio et al., 2019; Feng et al., 2023; Gardonio et al., 2018; Moore & Lockner, 2013; Nakagomi et al., 2021; Passelègue et al., 2018; Scuderi & Collettini, 2018; Sibson, 2000; Stabile et al., 2021; Verberne et al., 2015; Violay et al., 2014). Additionally, other studies have highlighted the occurrence of induced seismicity due to fluid injection, both during and after such operations (e.g., Albaric et al., 2014; Evans et al., 2005; Stanchits et al., 2011). The seismicity linked to fluid presence typically manifests as low magnitude events (e.g., Aochi et al., 2014; Leptokaropoulos et al., 2023; Passelègue et al., 2018; Stanton Yonge et al., 2025).

We propose that fluids lubricated faults and facilitated stress drops along the ATLFS over a prolonged 9 month period, during which the eastern sector of the ATLFS experienced significant acceleration relative to the western one. This fault rupture propagation differs from the common one, in which the co–seismic phase occurs through a mainshock lasting seconds to minutes, followed by an extended post–seismic phase, characterized by low–magnitude seismicity and gradual strain release, lasting from days to years. The two deformation types exhibit distinct trends in the GNSS position–time series. The conventional rupture propagation is represented by a curve with a peak corresponding to the co–seismic deformation, followed by a logarithmic or exponential decay curve that marks the gradual stress decrease during the post–seismic phase (e.g., Ergintav et al., 2009; Liu et al., 2024; Malservisi et al., 2015; Milliner et al., 2020; Wang et al., 2012). In contrast, the deformation regime, documented here, is described by a linear trend of the position–time curve in correspondence with the significant deformation event that occurred in 2021 (see blue bands in Figures 3a and 3b) and it is characterized by a continuous seismic strain release (Figures 7e and 7f) through low–magnitude events (Area 4a in Figure S3d in Supporting Information S1). Based on literature that correlates low–magnitude seismicity with fluid circulation (e.g., Aochi et al., 2014; Passelègue et al., 2018; Stanton Yonge et al., 2025), the observed increase in the frequency of low–magnitude events during the year 2021 could be indicative of enhanced fluid circulation in both the Vulcano area (Area 3, Figure S3c in Supporting Information S1) and the Peloritani Mts sector (Area 4a, Figure S3d in Supporting Information S1).

Compared to the pronounced trend variation observed in 2021, more minor variations were detected in the position–time series of Peloritani Mts stations (MUCR and MILA, yellow bands in Figures 3b and 3c) during 2017 and 2018. Similar to the 2021 event, these earlier changes show a temporal correlation with two key factors: (a) increased strain release in 2017 and 2018 across areas including the ATLFS, as indicated by jumps in the blue curve of Figure 7f for 2017 and the purple curves of Figures 7e and 7f for 2018, and (b) inflation events at Vulcano in 2017 and 2018 (Figure 5), which were accompanied by heightened CO_2 emissions during those years (see peaks in the curve of Figure 1c). Based on these correlations, we hypothesize that these variations in the deformation pattern of the ATLFS during 2017 and 2018 are also likely driven by enhanced fluid circulation, consistent with the mechanisms observed in 2021.

Significant variations in the position–time series of GNSS data were observed at the Salina and Lipari stations in 2021 along the Aeolian archipelago. At the Salina station, changes were detected primarily in the horizontal components (Figure 4c), whereas at the Lipari station, variations were recorded in the east and up components (Figure 4d). These anomalies cannot be conclusively attributed to the activation of fault systems between the Filicudi and Salina islands, or between the Salina and Lipari islands (see Section 5.1). Instead, it is plausible that these GNSS stations captured movements associated with hydrothermal fluid circulation, a phenomenon well documented for both Lipari (Decrée et al., 2005) and Salina islands (Italiano & Caruso, 2011). Notably, the Lipari station recorded a horizontal velocity of 20.4 mm/year toward the east (N82) in 2021 (Vita et al., 2012) a value significantly exceeding the typical tectonic deformation rates of a few mm/year observed in the study area. This suggests that localized processes, such as fluid dynamics and volcanic activity, played a critical role in driving these deformation patterns.

6. Conclusions

GNSS and seismological data from the Peloritani Mts and the central and western sectors of the Aeolian Archipelago allowed us to identify four deformation zones, characterized by WNW-ESE to NNW-SSE orientation and right-lateral kinematics, and detect the depths at which seismic strain is released. Furthermore, our findings provide new insights into the deformation timing and the magnitude of seismic events, particularly when fault reactivation is influenced by enhanced fluid circulation. The main outcomes are summarized as follow:

1. GNSS data analysis on Vulcano Island revealed periods of rapid ground inflation in 2017, 2018, 2019 and 2021. These periods coincide with increased CO_2 flux emissions, highlighting the critical role of fluid circulation in driving the inflation of the volcanic edifice.
2. GNSS position–time series analysis from the Peloritani Mts area revealed periods of rapid increase in the southward velocity of the eastern block of the ATLFS. The most persistent and pronounced velocity anomaly was recorded throughout 2021, showing a significant increase from 1.6 ± 0.28 mm/y (pre–2021 baseline) to 3.3 ± 0.99 mm/y during the year of the event. This acceleration was quantified relative to the fixed western block of the ATLFS, which served as the kinematic reference frame.
3. The acceleration observed in the eastern block of the ATLFS, which occurred in 2021, was accompanied by increased seismic strain release and is temporally correlated to the most significant rapid ground inflation on Vulcano Island. This temporal correlation suggests that increased fluid pressure controlled not only the ground inflation on Vulcano Island (see point 1), but also the movement of upper–crust blocks along the ATLFS.
4. Fluids lubricate faults and enable stress drops along the ATLFS, driving a deformation regime characterized by low–magnitude seismicity and a prolonged 9 month period of significant slip acceleration in the eastern block of the ATLFS relative to the western block.
5. GNSS position–time series from the Peloritani Mts area recorded smaller velocity increases in 2017 and 2018 than the 2021 event. These earlier changes are correlated with an increase in seismic strain release across the

ATLFS and rapid inflation events at Vulcano Island, accompanied by heightened CO_2 emissions. Similar to the 2021 event, these velocity increases are likely linked to enhanced fluid circulation within the fault system.
6. Seismogenic layer depths of 8–20 km related to the WAFSs (between Alicudi-Filicudi islands and Filicudi-Salina islands) suggest that these fault systems function as lateral ramps that transfer displacement between Africa and Eurasia's crustal blocks, involved in ongoing convergence.
7. Based on its position, kinematics, and seismogenic layer depths (up to 13 km), the tectonic relationship between the fault system of the central Aeolian Archipelago (between Lipari and Salina islands) and the major structures of the ATLFS and WAFSs leads to two interpretations: the fault system could (a) represent a transfer zone in the frame of Africa-Europe convergence, or (b) constitute the northern extension of the ATLFS.

Conflict of Interest

The authors declare no conflicts of interest relevant to this study.

Data Availability Statement

All data supporting the findings of this study are openly available under a CC BY 4.0 license. The GNSS time series, areal variation, and geodetic velocity field for the Peloritani Mountains and Aeolian Archipelago (Central Mediterranean) are available via Figshare at https://doi.org/10.6084/m9.figshare.29069753. Earthquake locations for the period 2011–2023, used in the analysis, are accessible through OEDataRep—the Osservatorio Etneo Open Data Repository via Barberi et al. (2025).

Acknowledgments

We thank the technicians of the GNSS and seismic networks of the Istituto Nazionale di Geofisica e Vulcanologia for ensuring the continuous maintenance of the stations. This work was (partially) funded by the project "Monitoring Earth's Evolution and Tectonics"—MEET, within the framework of Piano Nazionale di Ripresa e Resilienza (PNRR), Mission 4, Component 2, Investment 3.1 "Fondo per la realizzazione di un sistema integrato di infrastrutture di ricerca e innovazione."

References

Aiuppa, A., Bitetto, M., Calabrese, S., Delle Donne, D., Lages, J., La Monica, F. P., et al. (2022). Mafic magma feeds degassing unrest at Vulcano Island, Italy. *Communications Earth & Environment*, *3*(1), 255. https://doi.org/10.1038/s43247–022–00589–1

Albaric, J., Oye, V., Langet, N., Hasting, M., Lecomte, I., Iranpour, K., et al. (2014). Monitoring of induced seismicity during the first geothermal reservoir stimulation at Paralana, Australia. *Geothermics*, *52*, 120–131. https://doi.org/10.1016/j.geothermics.2013.10.013

Alparone, S., Barberi, G., D'Amico, S., Di Grazia, G., Giampiccolo, E., Maiolino, V., et al. (2023). Aeolian Seismic Catalog 2000–2019 (AeolianSC_2000_2019) (Version 1) [Dataset]. *Istituto Nazionale di Geofisica e Vulcanologia (INGV)*. https://doi.org/10.13127/AEOLIAN/AEOLIANRSC2000_2019

Altamimi, Z., Métivier, L., Rebischung, P., Rouby, H., & Collilieux, X. (2017). ITRF2014 plate motion model. *Geophysical Journal International*, *209*(3), 1906–1912. https://doi.org/10.1093/gji/ggx136

Aochi, H., Poisson, B., Toussaint, R., Rachez, X., & Schmittbuhl, J. (2014). Self–induced seismicity due to fluid circulation along faults. *Geophysical Journal International*, *196*(3), 1544–1563. https://doi.org/10.1093/gji/ggt356

Azzaro, R., D'Amico, S., Mostaccio, A., Scarfì, L., Tuvè, T., & Manni, M. (2014). Terremoti con effetti macrosismici in Sicilia orientale nel periodo Gennaio 2009—Dicembre 2013. In *Quaderni di Geofisica* (Vol. 120, p. 57). Istituto Nazionale di Geofisica e Vulcanologia (INGV). https://doi.org/10.13127/qdg/120

Barbano, M. S., Bottari, A., Carveni, P., Cosentino, M., Federico, B., Fonte, G., et al. (1979). Macroseismic study of the Gulf of Patti earthquake in the geostructural frame of north–eastern Sicily. *Bollettino della Società geologica italiana*, *98*, 155–174.

Barberi, G., Di Grazia, G., Ferrari, F., Firetto Carlino, M., Giampiccolo, E., Maiolino, V., et al. (2020). Aeolian Islands Revised Seismic Catalog from 2020 (AeolianRSC2020) (Version 1) [Dataset]. *Istituto Nazionale di Geofisica e Vulcanologia (INGV)*. https://doi.org/10.13127/AEOLIAN/AEOLIANRSC2020

Barberi, G., Messina, D., Corradino, M., Bruno, V., Mattia, M., Patanè, D., et al. (2025). Earthquake locations in the Peloritani Mountains and Aeolian archipelago (NE Sicily) using a 3D velocity model during 2011-2023 (PelAeolianEQ3D_2011-2023) [Dataset]. *Istituto Nazionale di Geofisica e Vulcanologia (INGV)*. https://doi.org/10.13127/pelaeolianeq3d_2011-2023

Barberi, G., Patanè, D., & Scarfì, L. (2018). Tomographic images of tectonic and volcanic structures in eastern Sicily obtained by active and passive seismic data inversion. In *Paper Presented at the 36th General Assembly of the European Seismological Commission, Valletta, Malta, September 2–7, 2018*. ESC2018-S8-299.

Barreca, G., Bruno, V., Cultrera, F., Mattia, M., Monaco, C., & Scarfì, L. (2014). New insights in the geodynamics of the Lipari–Vulcano area (Aeolian Archipelago, southern Italy) from geological, geodetic and seismological data. *Journal of Geodynamics*, *82*, 150–167. https://doi.org/10.1016/j.jog.2014.07.003

Barreca, G., Scarfì, L., Cannavò, F., Koulakov, I., & Monaco, C. (2016). New structural and seismological evidence and interpretation of a lithospheric–scale shear zone at the southern edge of the Ionian subduction system (central–eastern Sicily, Italy). *Tectonics*, *35*(6), 1489–1505. https://doi.org/10.1002/2015TC004057

Barreca, G., Scarfì, L., Gross, F., Monaco, C., & De Guidi, G. (2019). Fault pattern and seismotectonic potential at the south–western edge of the Ionian Subduction system (southern Italy): New field and geophysical constraints. *Tectonophysics*, *761*, 31–45. https://doi.org/10.1016/j.tecto.2019.04.020

Benson, P. M., Austria, D. C., Gehne, S., Butcher, E., Harnett, C. E., Fazio, M., et al. (2020). Laboratory simulations of fluid–induced seismicity, hydraulic fracture, and fluid flow. *Geomechanics for Energy and the Environment*, *24*, 100169. https://doi.org/10.1016/j.gete.2019.100169

Billi, A., Barberi, G., Faccenna, C., Neri, G., Pepe, F., & Sulli, A. (2006). Tectonics and seismicity of the Tindari Fault System, southern Italy: Crustal deformations at the transition between ongoing contractional and extensional domains located above the edge of a subducting slab. *Tectonics*, *25*(2). https://doi.org/10.1029/2004TC001763

Billi, A., Cuffaro, M., Orecchio, B., Palano, M., Presti, D., & Totaro, C. (2023). Retracing the Africa–Eurasia nascent convergent boundary in the western Mediterranean based on earthquake and GNSS data. *Earth and Planetary Science Letters*, *601*, 117906. https://doi.org/10.1016/j.epsl.2022.117906

Billi, A., Presti, D., Faccenna, C., Neri, G., & Orecchio, B. (2007). Seismotectonics of the Nubia plate compressive margin in the south Tyrrhenian region, Italy: Clues for subduction inception. *Journal of Geophysical Research*, *112*(B8), B08302. https://doi.org/10.1029/2006JB004837

Bizzarri, A. (2012). The mechanics of lubricated faults: Insights from 3-D numerical models. *Journal of Geophysical Research*, *117*(B5), B05304. https://doi.org/10.1029/2011JB008929

Boehm, J., Werl, B., & Schuh, H. (2006). Troposphere mapping functions for GPS and very long baseline interferometry from European Centre for Medium-Range Weather Forecasts operational analysis data. *Journal of Geophysical Research*, *111*(B2), B02406. https://doi.org/10.1029/2005JB003629

Bonardi, G., Cavazza, W., Perrone, V., & Rossi, S. (2001). Calabria–Peloritani terrane and northern Ionian Sea. In *Anatomy of an Orogen: The Apennines and adjacent Mediterranean basins* (pp. 287–306). Springer. https://doi.org/10.1007/978–94–015–9829–3_17

Bos, M., & Fernandes, R. (2021). Hector user manual version 1.9 2021. Retrieved from https://segal.ubi.pt/wp–content/uploads/2021/05/hector_manual_1.9.pdf

Bos, M. S., Fernandes, R. M. S., Williams, S. D. P., & Bastos, L. (2013). Fast error analysis of continuous GNSS observations with missing data. *Journal of Geodesy*, *87*(4), 351–360. https://doi.org/10.1007/s00190–012–0605–0

Cannata, A., Diliberto, I. S., Alparone, S., Gambino, S., Gresta, S., Liotta, M., et al. (2012). Multiparametric approach in investigating volcano–hydrothermal systems: The case study of Vulcano (Aeolian Islands, Italy). *Pure and Applied Geophysics*, *169*(1–2), 167–182. https://doi.org/10.1007/s00024–011–0297–z

Capasso, G., Favara, R., Francofonte, S., & Inguaggiato, S. (1999). Chemical and isotopic variations in fumarolic discharge and thermal waters at Vulcano Island (Aeolian Islands, Italy) during 1996: Evidence of resumed volcanic activity. *Journal of Volcanology and Geothermal Research*, *88*(3), 167–175. https://doi.org/10.1016/S0377–0273(98)00111–5

Capasso, G., Federico, C., Madonia, P., & Paonita, A. (2014). Response of the shallow aquifer of the volcano–hydrothermal system during the recent crises at Vulcano Island (Aeolian Archipelago, Italy). *Journal of Volcanology and Geothermal Research*, *273*, 70–80. https://doi.org/10.1016/j.jvolgeores.2014.01.005

Carapezza, M., Nuccio, P. M., & Valenza, M. (1981). Genesis and evolution of the fumaroles of Vulcano (Aeolian Islands, Italy): A geochemical model. *Bulletin Volcanologique*, *44*(3), 547–563. https://doi.org/10.1007/BF02600585

Carminati, E., & Doglioni, C. (2005). *EUROPE | Mediterranean tectonics, encyclopedia of geology*. Academic Press. https://doi.org/10.1016/B0-12-369396-9/00135-0

Carminati, E., Wortel, M. J. R., Spakman, W., & Sabadini, R. (1998). The role of slab detachment processes in the opening of the western–central Mediterranean basins: Some geological and geophysical evidence. *Earth and Planetary Science Letters*, *160*(3–4), 651–665. https://doi.org/10.1016/S0012–821X(98)00118–6

Castelblanco, C. A., Vargas, C. A., & Cardozo, N. (2025). Seismic attenuation in the Middle Magdalena Valley, Colombia, and possible relation to fluid lubricated fault zones. *Journal of South American Earth Sciences*, *153*, 105359. https://doi.org/10.1016/j.jsames.2025.105359

Castro–Melgar, I., Prudencio, J., Cannata, A., Del Pezzo, E., & Ibáñez, J. M. (2021). Small–scale volcanic structures of the Aeolian volcanic arc revealed by seismic attenuation. *Frontiers in Earth Science*, *9*, 725402. https://doi.org/10.3389/feart.2021.725402

Chiodini, G., Cioni, R., Falsaperla, S., Montalto, A., Guidi, M., & Marini, L. (1992). Geochemical and seismological investigations at Vulcano (Aeolian Islands) during 1978–1989. *Journal of Geophysical Research*, *97*(B7), 11025–11032. https://doi.org/10.1029/92JB00518

Cioni, R., & D'Amore, F. (1984). A genetic model for the crater fumaroles of Vulcano Island (Sicily, Italy). *Geothermics*, *13*(4), 375–384. https://doi.org/10.1016/0375–6505(84)90051–8

Cornelio, C., Spagnuolo, E., Di Toro, G., Nielsen, S., & Violay, M. (2019). Mechanical behaviour of fluid–lubricated faults. *Nature Communications*, *10*(1), 1274. https://doi.org/10.1038/s41467–019–09293–9

Corradino, M., Balazs, A., Faccenna, C., & Pepe, F. (2022). Arc and forearc rifting in the Tyrrhenian subduction system. *Scientific Reports*, *12*(1), 4728. https://doi.org/10.1038/s41598–022–08562–w

Corradino, M., Pepe, F., Bertotti, G., Picotti, V., Monaco, C., & Nicolich, R. (2020). 3-d architecture and Plio-Quaternary evolution of the Paola basin: Insights into the forearc of the Tyrrhenian-Ionian subduction system. *Tectonics*, *39*(2), e2019TC005898. https://doi.org/10.1029/2019TC005898

Cultrera, F., Barreca, G., Ferranti, L., Monaco, C., Pepe, F., Passaro, S., et al. (2017). Structural architecture and active deformation pattern in the northern sector of the Aeolian–Tindari–Letojanni fault system (SE Tyrrhenian Sea–NE Sicily) from integrated analysis of field, marine geophysical, seismological and geodetic data. *Italian Journal of Geosciences*, *136*(3), 399–417. https://doi.org/10.3301/IJG.2016.17

De Astis, G., Ventura, G., & Vilardo, G. (2003). Geodynamic significance of the Aeolian volcanism (Southern Tyrrhenian Sea, Italy) in light of structural, seismological, and geochemical data. *Tectonics*, *22*(4). https://doi.org/10.1029/2003TC001506

Decrée, S., Bernard, A., Yans, J., & De Putter, T. (2005). Poly–phase alteration history of the kaolinitized "Cava di Caolino" volcanics (Lipari Island, southern Italy). *Clay Minerals*, *40*(2), 153–165. https://doi.org/10.1180/0009855054020162

Dellong, D., Klingelhoefer, F., Kopp, H., Graindorge, D., Margheriti, L., Moretti, M., et al. (2018). Crustal structure of the Ionian basin and eastern Sicily margin: Results from a wide-angle seismic survey. *Journal of Geophysical Research: Solid Earth*, *123*(3), 2090–2114. https://doi.org/10.1002/2017JB015312

De Ritis, R., & Chiappini, M. (2023). High resolution magnetic anomalies, volcanism and tectonics of the active "La Fossa" vulcanic system (Vulcano island) and Lipari island (South Italy). *Journal of Volcanology and Geothermal Research*, *438*, 107823. https://doi.org/10.1016/j.jvolgeores.2023.107823

De Ritis, R., Ravat, D., Ventura, G., & Chiappini, M. (2013). Curie isotherm depth from aeromagnetic data constraining shallow heat source depths in the central Aeolian Ridge (Southern Tyrrhenian Sea, Italy). *Bulletin of Volcanology*, *75*(4), 710. https://doi.org/10.1007/s00445–013–0710–9

Diliberto, I. S. (2017). Long–term monitoring on a closed–conduit volcano: A 25 year long time–series of temperatures recorded at La Fossa cone (Vulcano Island, Italy), ranging from 250°C to 520°C. *Journal of Volcanology and Geothermal Research*, *346*, 151–160. https://doi.org/10.1016/j.jvolgeores.2017.03.005

Diliberto, I. S., Di Figlia, M. G., Cosenza, P., Foresta Martin, L., Francofonte, V., Mastrolia, A., et al. (2024). Temperatures recorded from January 2019 to February 2023 in the high–temperature fumaroles of the active cone of La Fossa Caldera. *Bulletin of Volcanology*, *86*(4), 30. https://doi.org/10.1007/s00445–024–01720–0

Di Luccio, F., Persaud, P., Cucci, L., Esposito, A., Carniel, R., Cortés, G., et al. (2021). The seismicity of Lipari, Aeolian Islands (Italy) from one–month recording of the LIPARI array. *Frontiers in Earth Science*, *9*, 678581. https://doi.org/10.3389/feart.2021.678581

Di Traglia, F., Bruno, V., Casu, F., Cocina, O., De Luca, C., Giudicepietro, F., et al. (2023). Multi-temporal InSAR, GNSS and seismic measurements reveal the origin of the 2021 Vulcano Island (Italy) Unrest. *Geophysical Research Letters*, *50*(24), e2023GL104952. https://doi.org/10.1029/2023GL104952

Donato, A., Tassi, F., Pecoraino, G., Manzella, A., Vaselli, O., Gagliano Candela, E., et al. (2021). Geochemical investigations of the geothermal systems from the Island of Sicily (southern Italy). *Geothermics*, *95*, 102120. https://doi.org/10.1016/j.geothermics.2021.102120

Ergintav, S., McClusky, S., Hearn, E., Reilinger, R., Cakmak, R., Herring, T., et al. (2009). Seven years of postseismic deformation following the 1999, M = 7.4 and M = 7.2, Izmit-Düzce, Turkey earthquake sequence. *Journal of Geophysical Research*, *114*(B7), B07403. https://doi.org/10.1029/2008JB006021

Evans, K. F., Genter, A., & Sausse, J. (2005). Permeability creation and damage due to massive fluid injections into granite at 3.5 km at Soultz: 1. Borehole observations. *Journal of Geophysical Research*, *110*(B4), B04203. https://doi.org/10.1029/2004JB003168

Faccenna, C., Becker, T. W., Lucente, F. P., Jolivet, L., & Rossetti, F. (2001). History of subduction and back arc extension in the Central Mediterranean. *Geophysical Journal International*, *145*(3), 809–820. https://doi.org/10.1046/j.0956–540x.2001.01435.x

Faccenna, C., Funiciello, F., Civetta, L., D'Antonio, M., Moroni, M., & Piromallo, C. (2007). Slab disruption, mantle circulation, and the opening of the Tyrrhenian basins. In *Cenozoic volcanism in the Mediterranean Area*. Geological Society of America. https://doi.org/10.1130/2007.2418(08)

Faccenna, C., Funiciello, F., Giardini, D., & Lucente, P. (2001). Episodic back–arc extension during restricted mantle convection in the Central Mediterranean. *Earth and Planetary Science Letters*, *187*(1–2), 105–116. https://doi.org/10.1016/S0012–821X(01)00280–1

Faccenna, C., Molin, P., Orecchio, B., Olivetti, V., Bellier, O., Funiciello, F., et al. (2011). Topography of the Calabria subduction zone (southern Italy): Clues for the origin of Mt. Etna. *Tectonics*, *30*(1). https://doi.org/10.1029/2010TC002694

Favalli, M., Karátson, D., Mazzuoli, R., Pareschi, M. T., & Ventura, G. (2005). Volcanic geomorphology and tectonics of the Aeolian archipelago (Southern Italy) based on integrated DEM data. *Bulletin of Volcanology*, *68*(2), 157–170. https://doi.org/10.1007/s00445–005–0429–3

Federico, C., Cocina, O., Gambino, S., Paonita, A., Branca, S., Coltelli, M., et al. (2023). Inferences on the 2021 ongoing volcanic unrest at Vulcano Island (Italy) through a comprehensive multidisciplinary surveillance network. *Remote Sensing*, *15*(5), 1405. https://doi.org/10.3390/rs15051405

Feng, W., Yao, L., Cornelio, C., Gomila, R., Ma, S., Yang, C., et al. (2023). Physical state of water controls friction of gabbro–built faults. *Nature Communications*, *14*(1), 4612. https://doi.org/10.1038/s41467–023–40313–x

Forni, F., Lucchi, F., Peccerillo, A., Tranne, C. A., Rossi, P. L., & Frezzotti, M. L. (2013). Chapter 10 stratigraphy and geological evolution of the Lipari volcanic complex (central Aeolian archipelago). *Geological Society, London, Memoirs*, *37*(1), 213–279. https://doi.org/10.1144/M37.10

Gardonio, B., Jolivet, R., Calais, E., & Leclère, H. (2018). The April 2017 Mw 6.5 Botswana Earthquake: An intraplate event triggered by deep fluids. *Geophysical Research Letters*, *45*(17), 8886–8896. https://doi.org/10.1029/2018GL078297

Gasparini, C., Iannaccone, G., & Scarpa, R. (1985). Fault–plane solutions and seismicity of the Italian Peninsula. *Tectonophysics*, *117*(1–2), 59–78. https://doi.org/10.1016/0040-1951(85)90236-7

Gasparini, C., Iannacone, G., Scandone, P., & Scarpa, R. (1982). Seismotectonics of the Calabrian arc. *Tectonophysics*, *82*, 267–286.

Giammanco, S., Palano, M., Scaltrito, A., Scarfì, L., & Sortino, F. (2008). Possible role of fluid overpressure in the generation of earthquake swarms in active tectonic areas: The case of the Peloritani Mts. (Sicily, Italy). *Journal of Volcanology and Geothermal Research*, *178*(4), 795–806. https://doi.org/10.1016/j.jvolgeores.2008.09.005

Gioncada, A., Mazzuoli, R., Bisson, M., & Pareschi, M. T. (2003). Petrology of volcanic products younger than 42 ka on the Lipari–Vulcano complex (Aeolian Islands, Italy): An example of volcanism controlled by tectonics. *Journal of Volcanology and Geothermal Research*, *122*(3–4), 191–220. https://doi.org/10.1016/S0377–0273(02)00502–4

Goes, S., Giardini, D., Jenny, S., Hollenstein, C., Kahle, H. –G., & Geiger, A. (2004). A recent tectonic reorganization in the south–central Mediterranean. *Earth and Planetary Science Letters*, *226*(3), 335–345. https://doi.org/10.1016/j.epsl.2004.07.038

Govers, R., & Wortel, M. J. R. (2005). Lithosphere tearing at STEP faults: Response to edges of subduction zones. *Earth and Planetary Science Letters*, *236*(1), 505–523. https://doi.org/10.1016/j.epsl.2005.03.022

Herring, T. (2003). MATLAB Tools for viewing GPS velocities and time series. *GPS Solutions*, *7*(3), 194–199. https://doi.org/10.1007/s10291–003–0068–0

Herring, T. A., King, R. W., Floyd, M. A., & McClusky, S. C. (2015). GLOBK reference manual. In *Global Kalman filter VLBI and GPS analysis program Release 10.6* (pp. 1–95).

Herring, T. A., King, R. W., Floyd, M. A., & Mcclusky, S. C. (2018b). GAMIT reference manual. In *GPS Analysis at MIT Release 10.7* (pp. 1–168).

Herring, T. A., King, R. W., Floyd, M. A., Mcclusky, S. C., & Sciences, P. (2018a). Introduction to GAMIT/GLOBK release 10.7 (pp. 1–168).

Inguaggiato, S., Calderone, L., Inguaggiato, C., Mazot, A., Morici, S., & Vita, F. (2012). Long–time variation of soil CO_2 fluxes at the summit crater of Vulcano (Italy). *Bulletin of Volcanology*, *74*(8), 1859–1863. https://doi.org/10.1007/s00445–012–0637–6

Inguaggiato, S., Mazot, A., Diliberto, I. S., Inguaggiato, C., Madonia, P., Rouwet, D., & Vita, F. (2012). Total CO_2 output from Vulcano Island (Aeolian Islands, Italy). *Geochemistry, Geophysics, Geosystems*, *13*(2), Q02012. https://doi.org/10.1029/2011GC003920

Inguaggiato, S., Vita, F., Diliberto, I. S., Inguaggiato, C., Mazot, A., Cangemi, M., & Corrao, M. (2022). The volcanic activity changes occurred in the 2021–2022 at Vulcano Island (Italy), inferred by the abrupt variations of soil CO_2 output. *Scientific Reports*, *12*(1), 21166. https://doi.org/10.1038/s41598–022–25435–4

Italiano, F., & Caruso, C. (2011). Detection of fresh and thermal waters over an island with extinct volcanism: The Island of Salina (Aeolian arc, Italy). *Procedia Earth and Planetary Science*, *4*, 39–49. https://doi.org/10.1016/j.proeps.2011.11.005

Kall, T., Oja, T., Kollo, K., & Liibusk, A. (2019). The noise properties and velocities from a time–series of Estonian permanent GNSS stations. *Geosciences*, *9*(5), 233. https://doi.org/10.3390/geosciences9050233

Lanzafame, G., & Bousquet, J. C. (1997). The Maltese escarpment and its extension from Mt. Etna to Aeolian Islands (Sicily): Importance and evolution of a lithosphere discontinuity. *Acta Vulcanologica*, *9*, 113–120.

Leptokaropoulos, K., Rychert, C. A., Harmon, N., Schlaphorst, D., Grevemeyer, I., Kendall, J. M., & Singh, S. C. (2023). Broad fault zones enable deep fluid transport and limit earthquake magnitudes. *Nature Communications*, *14*(1), 5748. https://doi.org/10.1038/s41467-023-41403-6

Liu, X., Deng, D., Jia, Z., Liu–Zeng, J., Mo, X., Huang, Y., et al. (2024). Refined coseismic slip model and surface deformation of the 2021 Maduo Earthquake: Implications for sensitivity of rupture behaviors to geometric complexity. *Remote Sensing*, *16*(4), 713. https://doi.org/10.3390/rs16040713

Lo Mauro, G., Gasperini, L., Sgroi, T., Barberi, G., & Polonia, A. (2025). Morphotectonics of the Gulf of Patti (Southern Tyrrhenian Sea) through pseudo-3D geophysical techniques. *Marine Geophysical Researches*, *46*(4), 35. https://doi.org/10.1007/s11001-025-09596-1

Lucente, F. P., Chiarabba, C., Cimini, G. B., & Giardini, D. (1999). Tomographic constraints on the geodynamic evolution of the Italian region. *Journal of Geophysical Research*, *104*(B9), 20307–20327. https://doi.org/10.1029/1999JB900147

Lyard, F., Lefevre, F., Letellier, T., & Francis, O. (2006). Modelling the global ocean tides: Modern insights from FES2004. *Ocean Dynamics*, *56*(5–6), 394–415. https://doi.org/10.1007/s10236–006–0086–x

Maesano, F. E., Tiberti, M. M., & Basili, R. (2017). The Calabrian Arc: Three–dimensional modelling of the subduction interface. *Scientific Reports*, *7*(1), 8887. https://doi.org/10.1038/s41598–017–09074–8

Malservisi, R., Schwartz, S. Y., Voss, N., Protti, M., Gonzalez, V., Dixon, T. H., et al. (2015). Multiscale postseismic behavior on a megathrust: The 2012 Nicoya earthquake, Costa Rica. *Geochemistry, Geophysics, Geosystems*, *16*(6), 1848–1864. https://doi.org/10.1002/2015GC005794

Mazzuoli, R., Tortorici, L., & Ventura, G. (1995). Oblique rifting in Salina, Lipari and Vulcano islands (Aeolian islands, southern Italy). *Terra Nova*, *7*(4), 444–452. https://doi.org/10.1111/j.1365–3121.1995.tb00540.x

Milliner, C., Bürgmann, R., Inbal, A., Wang, T., & Liang, C. (2020). Resolving the kinematics and moment release of early afterslip within the first hours following the 2016 Mw 7.1 Kumamoto Earthquake: Implications for the shallow slip deficit and frictional behavior of aseismic creep. *Journal of Geophysical Research: Solid Earth*, *125*(9), e2019JB018928. https://doi.org/10.1029/2019JB018928

Moore, D. E., & Lockner, D. A. (2013). Chemical controls on fault behavior: Weakening of serpentinite sheared against quartz-bearing rocks and its significance for fault creep in the San Andreas system. *Journal of Geophysical Research: Solid Earth*, *118*(5), 2558–2570. https://doi.org/10.1002/jgrb.50140

Nakagomi, K., Terakawa, T., Matsumoto, S., & Horikawa, S. (2021). Stress and pore fluid pressure control of seismicity rate changes following the 2016 Kumamoto earthquake, Japan. *Earth Planets and Space*, *73*(1), 11. https://doi.org/10.1186/s40623–020–01329–5

Neri, G., Caccamo, D., Cocina, O., & Montalto, A. (1996). Geodynamic implications of earthquake data in the southern Tyrrhenian Sea. *Tectonophysics*, *258*(1–4), 233–249. https://doi.org/10.1016/0040–1951(95)00202–2

Neri, G., Orecchio, B., Totaro, C., Falcone, G., & Presti, D. (2009). Subduction beneath southern Italy close the ending: Results from seismic tomography. *Seismological Research Letters*, *80*(1), 63–70. https://doi.org/10.1785/gssrl.80.1.63

Neri, G., Marotta, A. M., Orecchio, B., Presti, D., Totaro, C., Barzaghi, R., & Borghi, A. (2012). How lithospheric subduction changes along the Calabrian Arc in southern Italy: Geophysical evidences. *International Journal of Earth Sciences*, *101*(7), 1949–1969. https://doi.org/10.1007/s00531–012–0762–7

Nijholt, N., & Govers, R. (2015). The role of passive margins on the evolution of Subduction-Transform Edge Propagators (STEPs). *Journal of Geophysical Research: Solid Earth*, *120*(10), 7203–7230. https://doi.org/10.1002/2015JB012202

Ogniben, l. (1969). Schema introduttivo alla geologia del Confine calabro–lucano. *Bollettino della Società geologica italiana*, *8*, 453–763.

Palano, M., Ferranti, L., Monaco, C., Mattia, M., Aloisi, M., Bruno, V., et al. (2012). GPS velocity and strain fields in Sicily and southern Calabria, Italy: Updated geodetic constraints on tectonic block interaction in the central Mediterranean. *Journal of Geophysical Research*, *117*(B7), B07401. https://doi.org/10.1029/2012JB009254

Palano, M., Schiavone, D., Loddo, M., Neri, M., Presti, D., Quarto, R., et al. (2015). Active upper crust deformation pattern along the southern edge of the Tyrrhenian subduction zone (NE Sicily): Insights from a multidisciplinary approach. *Tectonophysics*, *657*, 205–218. https://doi.org/10.1016/j.tecto.2015.07.005

Passelègue, F. X., Brantut, N., & Mitchell, T. M. (2018). Fault reactivation by fluid injection: Controls from stress state and injection rate. *Geophysical Research Letters*, *45*(23), 12837–12846. https://doi.org/10.1029/2018GL080470

Pepe, F., Sulli, A., Bertotti, G., & Cella, F. (2010). Architecture and Neogene to Recent evolution of the western Calabrian continental margin: An upper plate perspective to the Ionian subduction system, central Mediterranean. *Tectonics*, *29*(3). https://doi.org/10.1029/2009TC002599

Pondrelli, S., Piromallo, C., & Serpelloni, E. (2004). Convergence vs. retreat in Southern Tyrrhenian Sea: Insights from kinematics. *Geophysical Research Letters*, *31*(6), L06611. https://doi.org/10.1029/2003GL019223

Rosenbaum, G., Gasparon, M., Lucente, F. P., Peccerillo, A., & Miller, M. S. (2008). Kinematics of slab tear faults during subduction segmentation and implications for Italian magmatism. *Tectonics*, *27*(2). https://doi.org/10.1029/2007TC002143

Rovida, A., Locati, M., Camassi, R., Lolli, B., Gasperini, P., & Antonucci, A. (2022). Catalogo Parametrico dei Terremoti Italiani (CPTI15), versione 4.0 [Dataset]. *Istituto Nazionale di Geofisica e Vulcanologia (INGV)*. https://doi.org/10.13127/cpti/cpti15.4

Sartori, R. (1990). The main results of ODP Leg 107 in the frame of Neogene to recent geology of Peri–Tyrrhenian areas. In *Proceedings of the Ocean Drilling Program, Scientific Results* (Vol. 107, pp. 715–730).

Scarfì, L., Barberi, G., Barreca, G., Cannavò, F., Koulakov, I., & Patanè, D. (2018). Slab narrowing in the Central Mediterranean: The Calabro–Ionian subduction zone as imaged by high resolution seismic tomography. *Scientific Reports*, *8*(1), 5178. https://doi.org/10.1038/s41598–018–23543–8

Scarfì, L., Barberi, G., Musumeci, C., & Patanè, D. (2016). Seismotectonics of northeastern Sicily and southern Calabria (Italy): New constraints on the tectonic structures featuring in a crucial sector for the central Mediterranean geodynamics. *Tectonics*, *35*(3), 812–832. https://doi.org/10.1002/2015TC004022

Scarfì, L., Messina, A., & Cassisi, C. (2013). Sicily and southern Calabria focal mechanism database: A valuable tool for local and regional stress-field determination. *Annals of Geophysics*, *56*(1), D0109. https://doi.org/10.4401/ag-6109

Scarfì, L., Raffaele, R., Badi, G., Ibáñez, J. M., & Imposa, S. (2012). Seismicity and crustal velocity structure of the Southern Central Andes—Western Argentina. In *Paper Presented at 5th EAGE St. Petersburg International Conference and Exhibition on Geosciences—Making the Most of the Earth Resources*. https://doi.org/10.3997/2214–4609.20143711

Scuderi, M. M., & Collettini, C. (2018). Fluid injection and the mechanics of frictional stability of shale-bearing faults. *Journal of Geophysical Research: Solid Earth*, *123*(10), 8364–8384. https://doi.org/10.1029/2018JB016084

Sibson, R. H. (2000). Fluid involvement in normal faulting. *Journal of Geodynamics*, *29*(3–5), 469–499. https://doi.org/10.1016/S0264–3707(99)00042–3

Stabile, T. A., Vlček, J., Wcisło, M., & Serlenga, V. (2021). Analysis of the 2016–2018 fluid–injection induced seismicity in the High Agri Valley (Southern Italy) from improved detections using template matching. *Scientific Reports*, *11*(1), 20630. https://doi.org/10.1038/s41598–021–00047–6

Stanchits, S., Mayr, S., Shapiro, S., & Dresen, G. (2011). Fracturing of porous rock induced by fluid injection. *Tectonophysics*, *503*(1–2), 129–145. https://doi.org/10.1016/j.tecto.2010.09.022

Stanton–Yonge, A., De La Muela, A. S., Pearce, R. K., Hammond, J. O., Mitchell, T. M., Hicks, S. P., et al. (2025). Fluid pressure fluctuations and the seismic signature of a fault–controlled fluid migration pulse. *Earth and Planetary Science Letters*, *662*, 119388. https://doi.org/10.1016/j.epsl.2025.119388

Ventura, G. (1994). Tectonics, structural evolution and caldera formation on Vulcano Island (Aeolian Archipelago, southern Tyrrhenian Sea). *Journal of Volcanology and Geothermal Research*, *60*(3–4), 207–224. https://doi.org/10.1016/0377-0273(94)90052-3

Ventura, G., Vilardo, G., Milano, G., & Pino, N. A. (1999). Relationships among crustal structure, volcanism and strike–slip tectonics in the Lipari–Vulcano Volcanic Complex (Aeolian Islands, Southern Tyrrhenian Sea, Italy). *Physics of the Earth and Planetary Interiors*, *116*(1–4), 31–52. https://doi.org/10.1016/S0031–9201(99)00117–X

Verberne, B. A., Niemeijer, A. R., De Bresser, J. H. P., & Spiers, C. J. (2015). Mechanical behavior and microstructure of simulated calcite fault gouge sheared at 20–600°C: Implications for natural faults in limestones. *Journal of Geophysical Research: Solid Earth*, *120*(12), 8169–8196. https://doi.org/10.1002/2015JB012292

Verberne, B. A., van den Ende, M. P. A., Chen, J., Niemeijer, A. R., & Spiers, C. J. (2020). The physics of fault friction: Insights from experiments on simulated gouges at low shearing velocities. *Solid Earth*, *11*(6), 2075–2095. https://doi.org/10.5194/se–11–2075–2020

Violay, M., Di Toro, G., Nielsen, S., Spagnuolo, E., & Burg, J. P. (2015). Thermo–mechanical pressurization of experimental faults in cohesive rocks during seismic slip. *Earth and Planetary Science Letters*, *429*, 1–10. https://doi.org/10.1016/j.epsl.2015.07.054

Violay, M., Nielsen, S., Gibert, B., Spagnuolo, E., Cavallo, A., Azais, P., et al. (2014). Effect of water on the frictional behavior of cohesive rocks during earthquakes. *Geology*, *42*(1), 27–30. https://doi.org/10.1130/G34916.1

Vita, F., Inguaggiato, S., Bobrowski, N., Calderone, L., Galle, B., & Parello, F. (2012). Continuous SO_2 flux measurements for Vulcano Island, Italy. *Annals of Geophysics*, *55*(2). https://doi.org/10.4401/ag-5759

Wang, L., Hainzl, S., Zöller, G., & Holschneider, M. (2012). Stress- and aftershock-constrained joint inversions for coseismic and postseismic slip applied to the 2004 M6.0 Parkfield earthquake. *Journal of Geophysical Research*, *117*(B7), B07406. https://doi.org/10.1029/2011JB009017

Zhang, H., Thurber, C., & Bedrosian, P. (2009). Joint inversion for Vp, Vs, and Vp/Vs at SAFOD, Parkfield, California. *Geochemistry, Geophysics, Geosystems*, *10*(11), Q11002. https://doi.org/10.1029/2009GC002709